Chinese Journal of Chemical Engineering 53 (2023) 101–123

Contents lists available at ScienceDirect

Chinese Journal of Chemical Engineering

journal homepage: www.elsevier.com/locate/CJChE

Review

PtCo-based nanocatalyst for oxygen reduction reaction: Recent highlights on synthesis strategy and catalytic mechanism

Wenjuan Yan [1,*], Puhua Sun [1], Chen Luo [2], Xingfan Xia [1], Zhifei Liu [1], Yuming Zhao [1], Shuxia Zhang [1], Liang Sun [1], Feng Du [1]

[1] State Key Laboratory of Heavy Oil Processing, Center for Chemical Engineering Experimental Teaching, Oil Industry Training Center, China University of Petroleum, Qingdao 266580, China
[2] Petrochemical Research Institute, PetroChina, Beijing 102200, China

ARTICLE INFO

Article history:
Received 16 December 2021
Received in revised form 3 March 2022
Accepted 6 March 2022
Available online 26 April 2022

Keywords:
Electrochemistry
Catalysis
Oxygen reduction reaction
Fuel cells
PtCo nanoalloy
Multimetallic

ABSTRACT

Oxygen reduction reaction over Pt-based catalyst is one of the most significant cathode reactions in fuel cells. However, low reserves and high price of Pt have motivated researchers worldwide seeking enhanced utilization efficiency and durability by doping non-noble metals to form Pt-based alloy catalysts. Alloying Pt with Co has been recognized as one of the most effective approaches to achieve this goal. PtCo bimetal combination is one of the most promising candidates to synthesize highly efficient catalysts for oxygen reduction reaction (ORR) applications, owing to its relatively more suitable oxygen binding energy for four-electron transfer reactions. Recently, impressive strategies have been developed to fabricate more active and stable PtCo-based multimetallic alloys with tailorable size and morphology. This paper aims to summarize the most recent highlights on the study of the relationship between preparation strategies, morphologies, electroactivities of the PtCo-based catalyst at atomic level and further the relevant reaction mechanism. The challenges and opportunities on the further development of electrocatalysts for fuel cells are included to provide reference for the practical application.

1. Introduction

With increasing concerns on environmental pollution and overuse of fossil fuel resources caused by the surging growth of global energy demand, extensive attention has been put to develop cleaner, cheaper and more renewable energies to address these issues [1]. However, large-scale implementation of renewable energy network requires electrochemical energy conversion systems with high efficiency, high reliability, and low cost [2,3]. Fuel cell is recognized as one of the ideal environment-friendly energy conversion systems in the future, due to its high efficiency, remarkable environmental friendliness, and wide range of fuel choices, *e.g.*, hydrogen, natural gas, methane, and other hydrocarbons [4]. These advantageous features distinguish fuel cells from conventional energy conversion and electricity generation. The oxygen reduction reaction (ORR) is a crucial cathode reaction for fuel cell. However, the sluggish kinetics and high overpotential have restricted the practical applications of fuel cells in clean energy technology. Hence, designing highly active and stable electrocatalysts for the ORR has been recognized as a momentous task in the development of highly efficient and economic fuel cells [5–7].

Among other metal candidates, Pt-based nanocatalysts show the best overall catalytic activity for ORR [8]. However, the commercial Pt/C catalysts have high cost and significant performance degradation because of fast agglomeration and Ostwald ripening of Pt nanoparticles under long-term operation [4]. Hence, it is crucial to develop efficient, stable, and cost-effective catalysts for ORR to realize the widespread adoption of fuel cells. Alloying Pt with non-noble transition metals, *e.g.* Co [9–14], Cu [15–20], Fe [21–23], and Ni [24–32], is an effective approach to obtain highly active and cost-inexpensive electrocatalysts. The strain and synergetic effect due to the formation of bimetallic alloy can tune the adsorption of reactive molecules on catalyst surface and expose more active sites for surface reactions.

Among all non-noble metal species, cobalt-based nano-alloys have attracted a lot of experimental and theoretical attention owning to their potential technological applications in energy conversion and storage field [33–40]. Co metal is oxophilic and electropositive, abundant, inexpensive, which could change the oxygen binding energy, facilitate the four-electron transfer rate,

* Corresponding author.
E-mail address: wenjuanyan@upc.edu.cn (W. Yan).

https://doi.org/10.1016/j.cjche.2022.03.024
1004-9541/

and improve the catalytic activity for Pt-based catalysts [41]. Hence, PtCo-based alloys can be prepared by various methods, such as seeded growth [42], copolymer-mediated approach [43], sonoelectrochemistry [44], and solvothermal method [45] with improved ORR performances [46–51]. In this context, PtCo nanocatalysts with different structures have been widely studied, including nanoflowers [52,53], nanowires [54–57], nanodendrites [58–60], nanofilms [61-63], monolayer nanoparticles [64–66], core-shell nanoparticles [67–73], concave nanocube [74], octahedral nanoparticles [75,76], and dodecahedral nanoparticles [77–79]. PtCo nanoparticles are often immobilized on various kinds of carbon-based support, *e.g.* carbon black [80–83], graphene oxide [84–86], and carbon nanotube to increase the dispersion and stability [87–91]. PtCo based trimetallic catalysts also have been widely reported with high performances, *e.g.* PtCoNi [92–95], PtCoPd [96,97], PtCoSn [98], PtCoNb [99], PtCoIr [100,101], PtCoAg [102], PtCoCu [19,103], PtCoAu [104,105], PtCoMn [106], and PtCoFe [107,108].

Very limited articles have been reported to summarize the development of the synthesis techniques for Pt-based nanocatalysts with diverse morphologies and tunable compositions [109]. Zhang *et al.* [4] reviewed the progress in the synthesis of monometallic Pt-based catalysts and elaborated its reaction mechanism. In 2017, Fan *et al.* [110] reviewed the promising progress of Pt based catalyst, including some alloys (Pt/Pd, Pt/Ni), made in this field since 2011. In 2016, Chenitz *et al.* [10] thoroughly reviewed the recent advances in ORR for proton exchange membrane fuel cells (PEMFCs). Clearly, there is a lack of a comprehensive discussion on the latest progress of preparation strategies, morphology effect and plausible deactivation mechanism of PtCo based alloys for ORR application, even though PtCo catalysts have been viewed as most promising for fuel cells. Hence, this work will review and summarize the latest progress of PtCo based nanoparticles with controllable morphology and particle size for enhanced ORR performances. In particular, the following aspects will be highlighted and discussed critically, (a) the synthesis method and conditions, (b) role of the surfactant, reductant, solutions and metal precursors, (c) the effect of the morphology and support to the electrocatalytic activity of PtCo based alloy. This work will provide guiding information for design of highly efficient and durable electrocatalysts for fuel cells application.

2. Structure Effect of Binary PtCo Metallic Nanocatalysts for ORR

2.1. The fundamentals

The electrocatalysts were evaluated by measuring LSV curves over painted catalysts on the rotating disk electrode (RDE). The catalysts were usually mixed with ethanol/DI water/isopropanol (IPA) and Nafion solution, and dispersed on a glassy carbon RDE. The RDE was polished with Al_2O_3 before coating with catalyst. The as-prepared electrode was then tested in the solution of O_2-saturated $HClO_4$ solution. The current densities, half-wave potential ($E_{1/2}$), mass and specific activities were measured and compared with the commercial Pt/C catalysts. The ORR mechanism of two-electron and four-electron paths has been widely studied as the latter path is more favorable thermodynamically with OOH*, O*, OH* as active intermediates [111]. A full mechanism of parallel ORR pathways over Pt and Co-active sites has been developed with sequential combination of protons and electrons as shown in Fig. 1 (a), (b) [112]. In the case of Co-N-C active site, there are two plausible concurrent ORR paths that, $^*-(OOH)_{ads}$ can form $^*-(O)_{ads}$ and water (Fig. 1(a)) or H_2O_2 (Fig. 1(b)) [112]. Since Co sites are more dense than Pt sites, O_2 gas may contact with Co sites before contacting with Pt sites. Thus, the $^*-(OOH)_{ads}$ formed on Co sites can be converted to H_2O directly or converted to H_2O_2 and transferred to Pt sites to form H_2O indirectly. This mechanism described the synergistic effect between Pt and Co active sites very well. The theoretical calculation of the oxygen binding energy according to the reaction mechanism gives a volcano plot that the activity of ORR dependents on the hydroxyl intermediate binding energy (Fig. 1(c)) [111]. Pt-based catalysts located near the top of the volcano plot with a suitable oxygen binding energy might give the highest ORR activity. If the hydroxyl binding energy is too small, the reaction rate is controlled by the OH* reduction step. Otherwise, the reaction rate is controlled by the OOH* formation step [111].

2.2. Polyhedral PtCo nanoparticles

The experiment studies confirmed the excellent ORR catalytic performance of Pt-based catalysts with various morphologies, different Pt electronic structure, and different intermediate binding

(a)

$$O_2 + * + (H^+ + e^-) \rightarrow\ ^*-(OOH)_{ads}$$

$$^*-(OOH)_{ads} + (H^+ + e^-) \rightarrow\ ^*-(O)_{ads} + H_2O$$

$$^*-(O)_{ads} + (H^+ + e^-) \rightarrow\ ^*-(OH)_{ads}$$

$$^*-(OH)_{ads} + (H^+ + e^-) \rightarrow\ * + H_2O$$

(b)

$$O_2 + * + (H^+ + e^-) \rightarrow\ ^*-(OOH)_{ads}$$

$$^*-(OOH)_{ads} + (H^+ + e^-) \rightarrow\ * + H_2O_2$$

$$H_2O_2 + * \rightarrow\ ^*-2(OH)_{ads}$$

$$^*-2(OH)_{ads} + 2(H^+ + e^-) \rightarrow\ * + 2H_2O$$

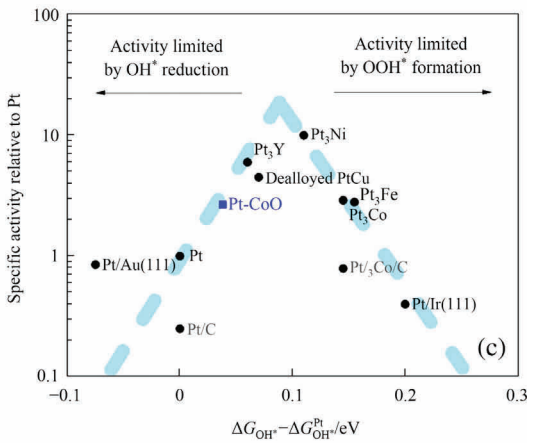

Fig. 1. (a) The full mechanism of ORR over Pt and Co-based catalysts [112], (b) the concurrent ORR path of Co-based active sites [112], (c) the ORR activity of Pt-based catalysts as a function of the hydroxyl intermediate binding energy, ΔG_{OH} [111].

energies. Pt_3Co was reported showing relatively higher activity than other 3d transition metals due to a weaker oxygen binding energy than Pt, and a down shift of the Pt d states relative to the Fermi level [113]. Concave cubic PtCo nanocrystals with Pt-rich surfaces (7–9 nm, Fig. 2(a)) were synthesized through a facile co-reduction strategy and tested for ORR in oxygen purged $HClO_4$ solution at a sweeping rate of 10 $mV{\cdot}s^{-1}$ [114]. Oeylamine (OAm) affected the uniformity of the shape and particle size significantly. Concave cubic PtCo/C catalyst displayed higher specific and mass activity (SA, MA, 2.7 and 1.9 times of Pt/C, Table 1, #1) than the spherical PtCo catalysts ascribing to the concave structure, Pt-rich surface, and alloyed composition. The durability test was carried out in 0.1 $mol{\cdot}L^{-1}$ oxygen saturated $HClO_4$ solution for 4000 cycles. The concave cubic PtCo catalyst displayed a 27% ECSA loss, which is lower than 35.3% ECSA loss of the Pt/C catalyst. The difference of atom size and electronic negativity between Co and Pt lead to the reducing of the d-band center of Pt, the rearrangement of the surface electrons of Pt lattices, the changing of the adsorption behaviors, and thus the increased activity and stability of the catalysts. Furthermore, the dissolution potential of PtCo surface is higher than the pure Pt surface, thus resulted in a higher stability [145].

Zheng's group [75] reported a simple cetyltrimethylammoniumbromide (CTAB)-assisted crystal growth method to synthesize PtCo alloy with an excavated octahedral shape (15 nm, Fig. 2(b)). The excavated octahedral PtCo alloy has larger electrochemically surface area (ECSA) compared to the normal octahedral PtCo alloy with the same size. The Br^- ions of CTAB play the key role in generating the excavated octahedral structure. The ORR cyclic voltammetry (CV) measurements were performed in a O_2-saturated 0.1 $mol{\cdot}L^{-1}$ $HClO_4$ solution at the scan rate of 10 $mV{\cdot}s^{-1}$. Owing to the combination of high surface area-to-volume ratio, active (100) facets and synergistic effect of Pt/Co, the excavated octahedral PtCo/C display 7.4 and 3.5 times higher SA and MA (Table 1, #2) than that of the Pt/C. In another work, highly ordered truncated cuboctahedral *cs*-Pt_3Co core-shell nanoparticles were synthesized (11.3 nm, Fig. 2(c)) [76]. EDS mapping confirmed the core-shell structure with a nearly complete Pt monolayer skin pro-

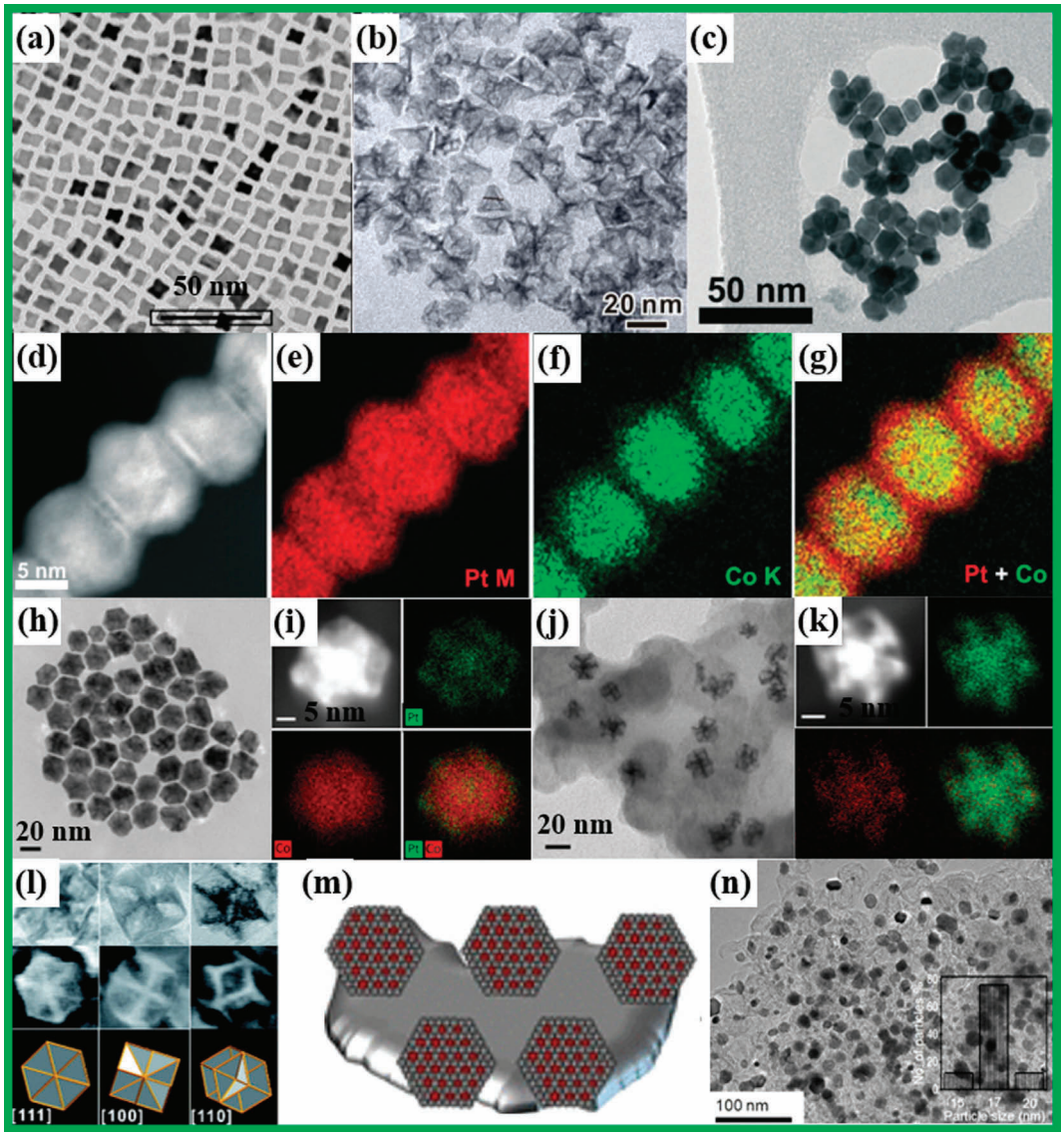

Fig. 2. TEM image of the (a) concave PtCo/C NPs [114], (b) excavated octahedral PtCo alloy NCs [75], (c) cuboctahedral *cs*-Pt_3Co [76], (d)–(g) HAADF STEM and EDS mapping of cuboctahedral *cs*-Pt_3Co [76], TEM images and EDS mapping of (h), (i) PtCo RD and (j), (k) PtCo NF [115], (l) TEM and SEM images of PtCo ERD NC, and the schematic models viewed along the (111), (100) and (110) directions [79], (m) schematic illustration of carbon supported Pt_3Co nanoplates [6], (n) low-magnification TEM image and the nanoparticle distribution of Pt_3Co/C [6].

Table 1
Summary of the synthesis conditions and catalytic performance of PtCo catalyst for ORR

#	Nanoalloy structure	Size/ nm	Precursor	Surfactant, solvent, reducing agent, additive	Temperature/ °C	Time/ h	MA to Pt/C	SA to Pt/C	Ref.
1	Concave cubic PtCo/CB	7–9	$Pt(acac)_2$, $Co_2(CO)_8$	1,2-hexadecane glycol, BE, OAm, OA	210	1.5	2	2	[114]
2	Octahedral PtCo/C	15.0	$Pt(acac)_2$, $Co(OAc)_2$	CTAB, DMF	180	15	3.5	7.4	[75]
3	Octahedral *cs*-PtCo/C	11.3	$Pt(acac)_2$, $Co(acac)_2$	DMF	140	20	–	6	[76]
4	Octahedral *ps*-PtCo/C	–	$Pt(acac)_2$, $Co(acac)_2$	DMF, H_2, Ar	700	2	–	1.2	[76]
5	Dodecahedral PtCo/C	23.0	H_2PtCl_6, $Co(acac)_2$	OAm, OA	240	0.1	4	6	[115]
6	PtCo ERD NC	38.4	H_2PtCl_6, $Co(acac)_2$	OAm, OA, formaldehyde	220	10	6	12	[79]
7	Hexagonal Pt_3Co/C nanoplate	17.0	Pt $(acac)_2$, $Co(acac)_2$	NaCl, KCl	800	3	8	21	[6]
8	Dendritic $Pt_{75}Co_{25}$	32.0	Pt $(acac)_2$, $Co(acac)_2$	CTAC, L-proline, OAm	180	8	2.8	–	[59]
9	Dendritic hierarchical Pt_4Co	50–200	Pt $(acac)_2$, $Co(acac)_2$	CTAC, citric acid, OAm	180	12	13.7	8.9	[116]
10	Dendritic PtCo/PPy	15.9	Pt $(acac)_2$, $Co(acac)_2$	CTAC, OAm, pyrrole monomer	160	8	1.8	–	[58]
11	Dendritic PtCo	14.0	K_2PtCl_4,$CoCl_2$	PVP, AA	200	6	9.3	6.7	[117]
12	Core-shell PtCo/C	6.2	H_2PtCl_6, $CoCl_2$	KOH, $NaBH_4$, EG	140	5	3.1	2.6	[118]
13	Core-shell PtCo/CB	2.5	$PtCl_4$, $CoCl_2$	$NaBH_4$, ethyl alcohol, sodium acetate, $HClO_4$	250	0.5	2	–	[119]
14	Core-shell PtCo/CB	2.5	$PtCl_4$, $CoCl_2$	OAm, EtOH, $NaBH_4$	80	1	1.8	1.2	[120]
15	Core-shell PtCo/C	8.0	$Co_2(CO)_8$, $Pt(acac)_2$	DCB, dioctylamine, oleic acid	160	4	8	10	[121]
16	Core-shell Co@PtC	10.0	H_2PtCl_6, $Co(NO_3)_2$	Ethanol, glucose, Na_2CO_3	180	8	5.8	5.4	[122]
17	Core-shell $L1_0$-CoPt/Pt/C	9.0	$Pt(acac)_2$, $Co(acac)_2$	OAm	300	60	19	38	[78]
18	$L1_0$-PtCo/C	4.6–5.8	$Pt(acac)_2$, $Co_2(CO)_8$	OAm, ODE	–	–	8.6	9	[123]
19	Core-shell $L1_0$-PtCo NPs	3.0	$Pt(acac)_2$, $Co(acac)_2$, $W(CO)_6$	OAm, ODE	–	–	18	19.5	[124]
20	PtCo NWs/C-hierarchical	–	$Pt(acac)_2$, $Co(acac)_2$	OAm, CTAC, glucose	160	8	33.7	39.6	[125]
21	PtCo NWs	2.0	$Pt(acac)_2$, $Co(acac)_2$	OAm, $Cr(CO)_6$	180	5	3.4	–	[55]
22	PtCo NWs	37.6	$Co(NO_3)_2$, K_2PtCl_4	$CO(NH_2)_2$, AA, KOH	50	–	6.3	1.0	[126]
23	Carbon nanotube supported PtCo	100	K_2PtCl_4, $CoCl_2$	F127, AA, KOH	RT	2	–	4.3	[89]
24	PtCo nanoflower	20.3	$Pt(acac)_2$, $Co(acac)_3$	OAm, CTAC	180	10	2.6	2	[127]
25	PtCo nanoflower	20.4	$Pt(acac)_2$, $Co(acac)_3$	OAm, CTAC, 1-nitroso-2-naphthol	180	12	5.6	–	[53]
26	PtCo nanoflower	25.4	$Pt(acac)_2$, $Co(acac)_3$	OAm, CTAC, glucose	200	10	1.8	–	[128]
27	PtCo nanoflower	–	$Pt(acac)_2$, $Co(acac)_3$	OAm, CTAC, L-glutamic acid	180	12	2	–	[45]
28	PtCo@N-GNS nanoflower	10.0	K_2PtCl_6, $Co(NO_3)_2$	ZIF-8	60	24	20.1	19.1	[129]
29	PtCo nanocubes/reduced graphene	34.0	$CoCl_2$,H_2PtCl_6	PVP, glycine, GO	200	9	–	6.7	[130]
30	PtCo/citric acid modified graphene	2.2	H_2PtCl_6, $CoCl_2$	EG, NaOH	130	3	3.2	2.8	[131]
31	PtCo/CNT	8.0	H_2PtCl_6	2-methylimidazole, PVP, methanol	80	24	4.8	–	[77]
32	H-PtCo@Pt/N-doped carbon	7.5	$Co(NO_3)_2$, K_2PtCl_4	2-methylimidazole, methanol, ethanol, water	RT	20	8	8	[132]
33	PtCo/Co/N-doped carbon	–	$Co(NO_3)_2$, H_2PtCl_6	2-methylimidazole, methanol, *n*-hexane, tannic acid, KOH	–	–	5.5	4.9	[133]
34	PtCo/N-doped carbon	–	H_2PtCl_6, $CoCl_2$	Polyacrylonitrile, NaOH	50	24	–	1.3	[134]
35	PtCo/ZIF	12.7	H_2PtCl_6, $Co(NO_3)_2$	PVP, ZIF-67	–	–	7.9	4.6	[135]
36	PtCo/ ZIF-67	7–10	$Co(NO_3)_2$, H_2PtCl_6	2-methylimidazole, methanol, ethanol	80	22	–	1.2	[136]
37	PtCoNi/ZIF	3.0	$Co(NO_3)_2$, $Ni(NO_3)_2$, H_2PtCl_6	2-methylimidazole, methanol	–	–	1.2	–	[28]
38	Core-shell PtCoAl/CB	4.0	H_2PtCl_6, $Co(NO_3)_2$	CB	950	15	20	13	[137]
39	PtCoRh-NDs	60.0	$Pt(acac)_2$, $Co(acac)_3$ Rh $(acac)_3$	CTAC, OAm	180	10	1.9	–	[138]
40	Cuboctahedron PtCoFe	5.5	$Pt(acac)_2$, $Co(acac)_2$, Fe $(acac)_3$,	CTAB, NaI	–	–	15.2	17.4	[107]
41	PtCoFe	5.0	$Pt(acac)_2$, $Co(acac)_2$, Fe $(acac)_3$,	Tetradecanediol, OA, DCB	200	2	4	–	[108]
42	Core-shell PtCoNi/CB	5.0	$Pt(acac)_2$, $Co(acac)_2$, Ni $(acac)_2$	PVP, glucose,1-octadecene, OAm	140	–	23	19	[139]
43	$L1_0$-$Co_1Ni_1Pt_2$/C	5.0	$Pt(acac)_2$, $Co(acac)_2$, Ni $(acac)_2$	OAm, BBA	300	1	31	58	[140]
44	$Pt(CoNi)_2$	63–73	$Pt(acac)_2$, $Co(Ac)_2$, Ni $(Ac)_2$	Trioctylamine, OAm, OA, 1-octadecene	300	0.3	10	5	[141]
45	PtCoNi	25.0	$Pt(acac)_2$, $Co(Ac)_2$, Ni $(Ac)_2$	PVP, KI, DMF	150	16	3.5	12.3	[29]
46	PtCoNi NW	0.8	$Pt(acac)_2$, $Ni(acac)_2$, Co $(acac)_3$	CTAC, $Mo(CO)_6$, OAm	160	2	32.3	26.9	[142]
47	PtCoAu/CB	5.6	$Pt(acac)_2$, $Co(acac)_2$, $KAuCl_4$	Acetone, CB, HNO_3	500	7	3.5	1.4	[143]
48	PtCoCu RNF	22.0	$Cu(OAc)_2$, $CoCl_2$, Pt $(acac)_2$	AA, OAm	250	–	5.4	16.8	[19]
49	PtCoW/graphene	2.9	H_2PtCl_6, $CoCl_2$, $W(CO)_6$	NaOH, EG	130	3	12	13	[144]

tecting the secondary shell of Pt_3Co and a Co-rich core (Fig. 2(d)–(g)). XPS indicated both oxidized and metallic states Co atoms existed in the *cs*-Pt_3Co nanocrystals. The SA of *cs*-Pt_3Co/C (1.44 mA·cm^{-2}, Table 1, #3) is 5 folds of the spherical *sp*-Pt_3Co/C (0.24 mA·cm^{-2}, Table 1, #4) and 6 folds of the Pt/C catalyst (0.22 mA·cm^{-2}) towards ORR. The durability test showed that there is only 11 mV negative shift in $E_{1/2}$ after 5000 cycles. Besides, the morphology for *cs*-Pt_3Co/C has no observable change, indicating the good stability of the catalyst.

Yang's group prepared PtCo nanoframes (PtCo NF) by etching the Co-rich phase of solid rhombic dodecahedra (PtCo RD) using nitric acid [115]. TEM images and EDS mapping outlined the structure of the solid PtCo RD at ~23 nm and hollow frame PtCo NF particles with Pt-rich phase on the edges (Fig. 2(h)–(k)). The obtained PtCo NF/C exhibit excellent ORR MA and SA (6 and 4 times, Table 1, #5) than commercial Pt/C in acidic electrolyte (0.1 mol·L^{-1} $HClO_4$) with negligible Co dissolution. The accelerated durability testing (ADT) after 10000 cycles showed that is 8% loss of ECSA in acidic conditions. The weakened oxygen binding energy and the downshift of the d-band center by the incorporation of Co are the main reason of better activity and stability. When the ORR test was carried out in alkaline KOH solution, the SA and MA of PtCo NF are 5 and 3 times higher than the commercial Pt/C catalyst. However, broken edges of PtCo NF and worse durability was noticed in KOH solution than that in $HClO_4$ due to the strong corrosion of KOH with the assistance of O_2. However, negligible Co dissolution was observed ascribing to the precorrosion with nitric acid. PtCo ERD NCs/C with excavated rhombic dodecahedral (ERD) structure were synthesized by Xie's group using wet chemical method (Fig. 2(l)) [79]. By tuning the Pt/Co ratio and the amount of formaldehyde, the convex structure evolved to excavated polyhedra. The SA and MA of as-prepared catalyst are almost 12 and 6 times higher than the commercial Pt/C for ORR, respectively (Table 1, #6).

The alloy structure, excavated morphology, less agglomeration, modified d-band center, synergetic effect, rearranged surface atoms, and the lattice strain of Pt are the reasons of higher activity and stability. Hexagonal Pt_3Co nanoplates with face center cubic (fcc) structure rather than L_{12} phase were synthesized by molten-salt synthesis method in the absence of capping agent [6]. Molten NaCl and KCl created a dense condition for forming the specific nanostructure. Fig. 2(m) displayed the schematic illustration of carbon supported Pt_3Co nanoplates. TEM images indicated a plate shape with 17 nm diameteer and 2 nm thickness (Fig. 2(n)). The MA and SA of hexagonal Pt_3Co/C nanoplates is 8 and 21 times higher than that of the commercial Pt/C catalyst attributing to the particle size effect, facets, and specific geometry (Table 1, #7). The incorporation of Co caused d-band shift of Pt and affected the Pt—OH, Pt—Pt, and Pt—Co band energy. This process followed a four-electron pathway for ORR as confirmed by the experimental study and calculation results. The durability test showed there is significant dissolution of the active metal after 40000 cycles.

We can conclude from the above discussion that excavated structure PtCo nanocrystals can provide higher activity than the non-excavated ones benefitting from the larger surface area. The structure direct agent and solvent have significant effect to the shape and size of the nanoparticles.

2.3. Dendritic PtCo nanoparticles

3D dendritic PtCo alloys have gained a lot attention due to the highly porous structure and large surface area on account of the numerous arms on every dendrite [146,147]. Detailed investigation by Wang *et al.* [59] showed uniform PtCo alloyed dendritic assemblies ($Pt_{75}Co_{25}$ NDAs) in the presence of OAm, cetyltrimethylammonium chloride (CTAC) and L-proline which played a role of reductant and structure directing agent. The well-defined dendritic architectures with an average size about 32 nm were confirmed by the STEM images (Fig. 3(a)–(b)). The concentration of CTAC has important effect to the morphology of the PtCo alloy. The formation mechanism showed that CTAC may coordinate with high-index facets of the precursors dissolved in OAm to liberated Cl^- which can coordinate to the (110) facet to form step surface. Pt nuclei formed at first place and facilitated the following Co salt reduction. The interaction between CTA^+ and L-proline may drive the oriented attachment of Pt and Co atoms to form self-assembled PtCo dendrites ($Pt_{75}Co_{25}$ NDAs) to reduce the total surface energy. The ORR polarization curves with this catalyst were recorded in O_2-saturated 0.5 mol·L^{-1} KOH. The $E_{1/2}$ of $Pt_{75}Co_{25}$ NDAs (0.95 V) is much larger than that of Pt black (PtB, 0.87 V). Furthermore, they obtained the electronic transfer number based on the K-L equation, which indicated a four-electron pathway and a direct reduction of O_2 to hydroxide species under alkaline conditions. The durability test showed there is small decline of the $E_{1/2}$ and nearly unchanged morphology after 1000 cycles. The good performance of $Pt_{75}Co_{25}$ NDAs (MA: 2.8 times of PtB, Table 1, #8) is benefited from the cooperative effects of the Pt and Co, and the dendritic structure with large surface area. To replace the L-proline with citric acid in above synthesis process, wave-like hierarchical Pt_4Co multidendrites (MDs) with rich defects and low coordinated atomic steps were produced using citric acid as an eco-friendly reducing agent (Fig. 3(c)) [116]. The appropriate citric acid concentration and the reaction temperature played the essential role of in the synthesis. The formation mechanism of Pt_4Co MDs is quite similar with that of $Pt_{75}Co_{25}$ NDAs [59]. The performance of Pt_4Co MDs for ORR was measured in O_2-saturated 0.1 mol·L^{-1} $HClO_4$, which displayed enhanced MA and SA (13.7 times of Pt/C, Table 1, #9) relative to the PtB due to enhanced diffusion of active species and suppressed Ostwald ripening. The other groups also provided evidence that forming surface defects is favorable to improve the electrocatalytic activity and structure integrity of intermetallic NPs [120,127,128,148]. They further investigated the ORR kinetics and obtained an electron transfer number of 4, indicating a four-electron pathway and direct reduction of oxygen to water. The accelerated durability test (ADT) of Pt_4Co MDs showed there is negligible difference of the $E_{1/2}$, but 19.8% and 19.9% decline of SA and MA after 1000 cycles. The decline of activity might be due to the aggregation and dissolution of the active metal species. Jung's group proposed the mechanism of Pt dissolution, that Pt leaching might occur as the reduction of Pt oxides by the following reactions: $PtO + 2H^+ \rightarrow Pt^{2+} + H_2O$, $PtO_2 + 4H^+ \rightarrow Pt^{4+} + 2H_2O$, $PtO_2 + 4H^+ + 2e^- \rightarrow Pt^{2+} + 2H_2O$ [38,149]. Jiang's group studied the degradation mechanism of PtCo/C and Pt/C catalyst (Fig. 3(e),(f)) [39]. For the Pt/C catalyst, they noticed the reduction of Pt sites and ORR activity due the structure transformation from partial-coverage PtO layer to the full-coverage PtO layer of the outer surface and partial-coverage of the subsurface PtO layer (Fig. 3(e)) [39]. For the PtCo/C catalyst, the outer Pt layer thickness increased due to the segregation and dissolution of CoO species (Fig. 3(f)) [39].

Dendritic PtCo nanoclusters immobilized on polypyrrole (PtCo/PPy, 15.86 nm, Fig. 3(d)) composing by several thin petals were reported by Wang's group [58]. Pyrrole and CTAC were applied as the reductant and capping agent, respectively. The Pt/Co ratio played an important role to form this structure by controlling the crystal growing process. Hence, the PtCo/PPy (178.91 mA·mg^{-1}, Table 1, #10) showed the best MA among Pt_3Co/PPy, $PtCo_3$/PPy and Pt/C catalysts (100.7 mA·mg^{-1}). Except for the metal composition, the enlarge ECSA with more active sites and the good conductivity of the PPy facilitated the catalytic performance. A one-step strategy was reported for synthesizing PtCo nanodendrites

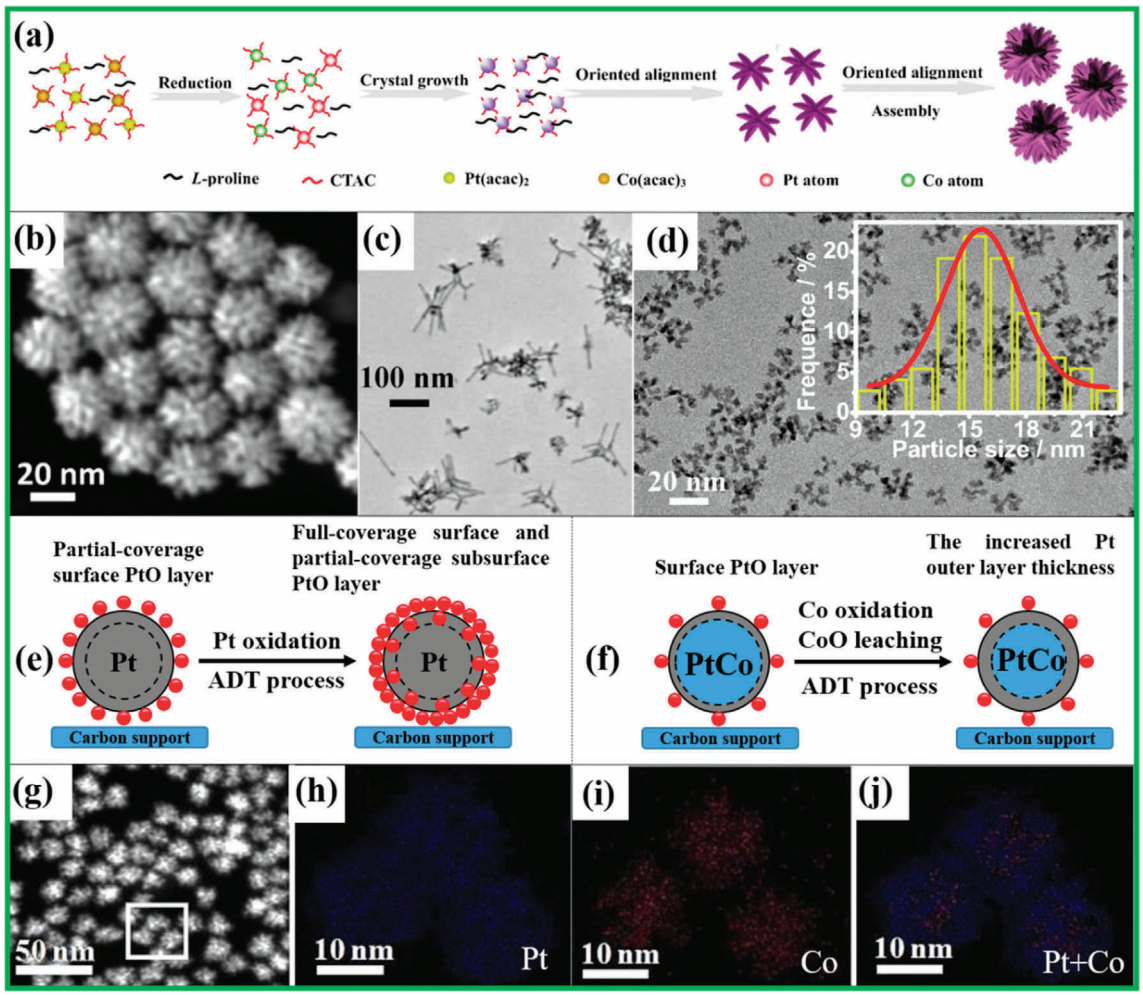

Fig. 3. (a) The formation mechanism of $Pt_{75}Co_{25}$ NDAs [59], HAADF-STEM image of (b) $Pt_{75}Co_{25}$ NDAs [59] and (e)–(g) PtCo nanodendrites [117], TEM image of (c) Pt_4Co MDs [116] and (d) dendritic PtCo NCs/PPy and particle size distribution [58], (h)–(j) EDS of PtCo nanodendrites [117], Degradation mechanism of the (e) Pt/C and (f) PtCo/C catalysts for ORR [39].

(14 nm, Fig. 3(g)–(j)) in aqueous solution without any organic solvent [117]. The presence of (111), (110), (100), (200), (220) and (311) facets are confirmed. The MA and SA of PtCo nanodendrites (1.21 $mA{\cdot}\mu g^{-1}$, 1.61 $mA{\cdot}cm^{-2}$, Table 1, #11) are 3 and 2.5 folds of the PtCo nanoflowers (0.45 $mA{\cdot}\mu g^{-1}$, 0.64 $mA{\cdot}cm^{-2}$) and 9.3 and 6.7 folds of the Pt/C (0.13 $mA{\cdot}\mu g^{-1}$, 0.24 $mA{\cdot}cm^{-2}$). The porous dendritic surface of PtCo nanodendrites provided abundant active sites for ORR. Furthermore, the presence of Co altered the electronic structure of Pt and prevented the formation of poisonous Pt oxides. According to the calculation of K-L equation, the electron transfer number is 4.06 for PtCo NCs/PPy, indicating a four-electron pathway for ORR. The ADT test showed the $E_{1/2}$ has a 9 mV shift, which is lower than 34 mV of Pt/C after 1000 cycles, indicating good stability of the PtCo NCs/PPy.

2.4. Core-shell PtCo nanoparticles

Core-shell PtCo alloy has special embedded porous structure, large specific surface area and thick Pt skin which can effectively protect the nanoparticles from aggregation and corrosion, thereby enhance the durability and activity for ORR [150]. Furthermore, atomistic simulations and DFT calculations suggested that the core–shell nanostructure prevent the dissolution of Co during the annealing process to maintain the bimetallic composition for catalytic activity enhancement.

Zhu *et al.* [118] synthesized carbon supported PtCo nanoparticles with stable Pt-rich shell and ordered Co core by a polyol reduction process. In this process, the annealing temperature was maintained at 700 °C to avoid unfavorable excessive particle growth at higher temperature. The as-synthesized PtCo NPs possess 8 nm-Co core and 1 nm-Pt shell as confirmed by the STEM and EDS. The XPS results indicated that high content of highly active metallic Pt^0 existed in the as-prepared PtCo catalysts. The electrochemical tests showed that the MA of Pt_3Co/C-700 (0.50 $A{\cdot}mg^{-1}$, Table 1, #12) is higher than that of the commercial Pt/C catalyst (0.16 $A{\cdot}mg^{-1}$) for ORR in O_2-saturated 0.1 $mol{\cdot}L^{-1}$ $HClO_4$ solution. They observed that by controlling the annealing temperature, they can obtain chemically ordered structure, of which the geometric and ligand effect increased the activity of the catalyst. The catalyst annealed at 700 °C has relatively higher degree of lattice contraction and more suitable binding energies. The electron transfer number for Pt_3Co/C-700 catalyst was calculated to be 4.0, indicating a four-electron pathway of ORR. The stability test showed Pt_3Co/C-700 has better structural stability even after 5000 cycles, due to the integrity of the Pt rich surface and ordered Co rich core. For core–shell PtCo nanocatalysts, the effect of post thermal annealing (PtCo-Pt-annealed) and additional Pt reduction (PtCo-Pt-chem) process to the catalytic activity have been studied [119]. The mass activities towards ORR are found to increase in the order of commercial Pt/C (3.5 nm, 0.19 $mA{\cdot}g^{-1}$) < PtCo-Pt/C (an-

nealed, 4.2 nm, 0.34 mA·g^{-1}) < PtCo–Pt/C (chem, 2.5 nm, 0.38 mA·g^{-1}, Table 1, #13). PtCo-Pt/C (chem) possessed much smoother and thicker Pt skin layer due to the extra Pt reduction than the PtCo-Pt/C (annealed). The thick Pt-skin prevented the Co leaching and improved the structure integrity of PtCo alloy at some degree as confirmed by XRD and XPS.

Bimetallic PtCo core were encapsulated in a stable Pt shell to obtain PtCo@Pt/C which displayed SA and MA of 1.2 and 1.8 times of the commercial Pt/C for ORR in PEMFCs (Fig. 4(a), Table 1, #14) [120]. In this synthesis process, the PtCo core was not damaged ascribing to the presence of hydride from Hantzsch ester, which concentrated Cl^- on the Pt frame and generated defects with negative charge. Bimetallic Pt_3Co nanoparticles with size around 4.96 nm was uniformly distributed on the surface of the shell isolated nanoparticles [151]. The obtained Pt_3Co catalyst showed a 5-fold improvement in activity compared to monometallic Pt catalyst due to the weak *O adsorption arise from electronic effect of PtCo alloy as confirmed by the DFT calculations. The presence of Co can generate strain and/or ligand effects and shift the Pt d-band to the Fermi level, thus change the Pt—O bond strength. A valid descriptor for the strain effects is the Pt —Pt bond distance which can be modified by changing the Co content [152]. Besides, they study the effect of pH on the performance of Pt_3Co for ORR. They observed that the Pt_3Co catalyst has inferior activity in alkaline solution compared to in the acid solution, due to the OH adsorption and CO segregation.

The core–shell Co@Pt nanoparticle with Pt shell (1 nm) and Co core (8 nm) preparing by Wang's group displayed 6.2 times improvement in catalytic activity (2.24 mA·cm^{-2}) *versus* commercial Pt/C catalysts (5 nm, 0.36 mA·cm^{-2}) in 0.1 mol·L^{-1} $HClO_4$ due to the larger particle size and electrochemically active surface area (ECSA, Table 1, #15) [121]. During the potential cycling study, dynamic surface restructuring was observed over Co@Pt catalyst due to dissolution, migration and redeposition of Pt on the surface. DFT calculation indicated that the Pt-skin surface has weaker binding with the OH, O, OOH, COOH, and CO groups comparing to the pure Pt species. As the thickness of Pt skin increases, the ORR activity increases at the beginning and declines after, following a volcano type of trend. When there is two-monolayer of Pt skin, the ORR activity reached the peak [121,153]. Compounding 2D sandwich-like Co@PtC samples (~10 nm) were synthesized by a general wet-chemical seed-medicated growth method [122]. The sample exhibited high activity and durability attributing to the carbon layer and Pt shell protection in 0.1 mol·L^{-1} O_2-saturated $HClO_4$ solution for ORR. Co@PtC samples with different thickness of Pt shell have different activities following the trend of Co@Pt/C-1 nm > Co@Pt/C-2 nm > Co@Pt/C-0.5 nm > Pt/C. The Co@Pt/C-1 nm catalyst has 5.8 and 5.4 times higher MA and SA activity than Pt/

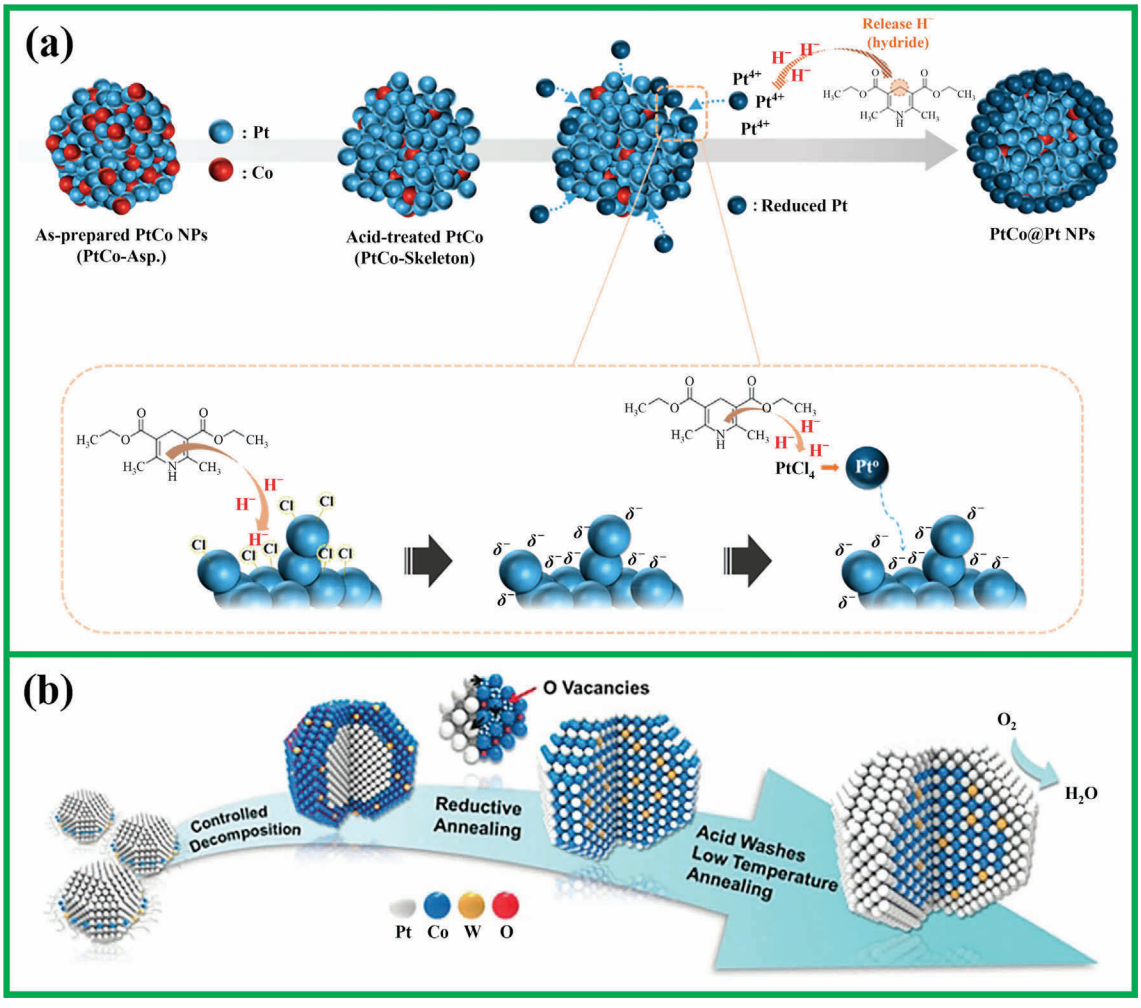

Fig. 4. (a) The synthesis process of PtCo@Pt NPs and the mechanism of anchoring additional Pt on defect sites [165], (b) Illustration of synthetic route to $L1_0$-W-PtCo NPs [149].

C (Table 1, #16, 0.21 A·mg^{-1}, 0.33 mA·cm^{-2}) and follows a four-electron pathway. The DFT calculations indicated that the compressive surface strain induced by Pt growing on the Co core has an essential role in reducing the absorption ability of the surface Pt atom (∼1 nm) and raising ORR activity. Furthermore, the Pt shell can protect the Co core from leaching out, thus improve the stability of the catalyst. The ADT study showed there is 19.8% and 12.7% decline of MA and SA after 40000 cycles, which is lower than 62.8% and 69.5% of Pt/C. PtCo alloy with Pt skin immobilizing on carbon with large surface area was prepared and evaluated for ORR in the presence of H_2SO_4 to study the effect of sulfate [154]. Pt-PtCo/C (3.3 nm) has 0.3–0.4 nm thick Pt layers (1–2 atomic) displayed about 2 times higher ORR activity and more tolerant to the trace amounts of sulfate than the commercial Pt/C under the operating conditions of fuel cells in the presence of H_2SO_4. In the absence of sulfate, O_2 tend to adsorb in the bridging configuration and form H_2O molecules *via* four-electron reduction. However, the sulfate may block the adsorption sites for O_2 adsorbing in a linear configuration in the presence of sulfate. Hence, the formation of H_2O_2 more likely undergo a two-electron reduction pathway.

Uchida's group successfully rearranged the fcc + fct (face centered tetragonal) structure to fcc phase by dissolving Co species of PtCo alloy [155]. The SA and durability of disordered fcc-Pt_3Co/C were higher than the ordered fct-Pt_3Co/C for ORR under the practical operation conditions of PEMFCs [156]. However, Sun's group observed that the fct CoPt/Pt showed higher activity than the etched fcc CoPt [78]. The fct-CoPt/Pt nanoparticles have hard-magnet core–shell structures with a shell being 2 ∼ 3 atoms thick of Pt. The mass and specific activities increased in the order of commercial Pt/C (0.12 mA·g^{-1}, 0.22 mA·cm^{-2}) < etched fcc-CoPt (0.15 mA·g^{-1}, 0.70 mA·cm^{-2}) < fct-CoPt/Pt (2.26 mA·g^{-1}, 8.26 mA·cm^{-2}, Table 1, #17). The $L1_0$ order core structure, the ligand effect and the Pt shell of the fct-CoPt/Pt can stabilize Co and weaken the oxygenated species-binding energetics on the Pt surface as confirmed by the DFT calculations [78]. In another work, the fcc PtCo nanocrystals (4–5 nm) have been transformed to the fct phase by thermal annealing to vary the concentration of Co in the system [123]. Increased ORR activity of PtCo/C was ascribing to the existence of fcc-PtCo and fct-PtCo phases as demonstrated with XRD (Table 1, #18) [123]. High temperature annealing may cause high degree of aggregation and particle size increasing. Carbon support and oxide coating can effectively control the particle size during the annealing process [157]. Sun's group applied a one-pot method to coat metal precursors with a layer of MgO to prevent PtFe NPs from sintering and particle size growing at high annealing temperatures [157]. Fujimori [158] and Huang's group [159] reported that SiO_2 could be used as coating to protect the particles from sintering during the annealing process. Furthermore, N-doped carbon coating also inhibit the coalescence and the metal dissolution [22]. Thus, it is easier to synthesize ordered metallic NPs with relatively small particle size by annealing process. W-doped ordered $L1_0$-PtCo nanocatalyst with ultrasmall particle size (3 nm) was synthesized by wet-chemical and high-temperature annealing method (Fig. 4(b)) [124]. $L1_0$-W-PtCo/C displayed good MA and SA which are 18 and 19.5 folds of the commercial Pt/C catalyst, respectively (Table 1, #19) [124]. The ADT test showed there is 7.7% loss of MA which is far less than the loss of the commercial Pt/C (26.9%). The good activity and stability are attributed to the Pt rich shell (2–3 atomic layer), ordered $L1_0$ structure, optimal Pt—Pt bond length and compressive strain on the catalyst surface. Ordered fct-PtCo/CCCS catalysts were oreoared by migrating the Co species in the N-doped carbon shell up to the Pt surface [160]. The MA of PtCo/CCCS catalyst (0.39 mA·g^{-1}) is three-fold to the commercial Pt/C (0.14 mA·g^{-1}). Ternary-fct ordered PtCoCu/C catalyst with high crystallinity and ordered crystal phase was reported exhibiting high MA and SA (1.31 mA·g^{-1}, 0.59 A·cm^{-2}) than commercial Pt/C catalyst [103]. The presence of Co and Cu modified the Pt—Pt bond length and retained the ordered phase under acid environment, thus improved the electrochemical activities. The associative and dissociative mechanisms on $L1_0$–PtCo/Pt (111) surfaces for ORR were explored by DFT calculation [161]. The fct–PtCo/Pt (111) surfaces showed superior activity for ORR comparing to the fcc Pt (111) surface attributing to the weaker bond between the reaction intermediates and the fct-PtCo/Pt surfaces comparing to the fcc Pt (111) surface. Furthermore, they also noticed that the strain and ligand effects become dominant to the ORR activity for Pt over layer thickness of more than three atomic shell layers. Wu *et al.* [162] also came to the same conclusion when they calculated the adsorption energies of OH, OOH, and O on various tetragonal structured alloy with Pt skins to understand the fct structures. The geometrical role of the fct core indicated that other non-Pt fct structures can be adopted as the core to further reduce the composition of Pt. Core-shell Pt-PtCo/GCB were prepared and supported on graphitized carbon black by depositing additional Pt layer on Co-enriched nanocore with two layers of Pt [163]. Pt-PtCo/GCB provided three times higher MA of a commercial Pt/C catalyst for the ORR. Gan's group also prepared a carbon supported $PtCo_3$ with durably thin Pt shells (<0.6 nm) by high temperature thermal annealing [164]. The $PtCo_3$ annealed at 600 °C showed a slightly larger particle size (5.1 nm) but enhanced activity (740 mA·mg^{-1}, 1.74 mA·cm^{-2}) compared to the $PtCo_3$ annealed at 400 °C (630 mA·mg^{-1}, 1.18 mA·cm^{-2}) and the Pt/C catalyst. The durable thin Pt shells and the ordered core with high Co content are viewed as the main reason of the high performance.

The synthesis of core shell structure nanoparticles is a feasible method to improve the durability of PtCo based alloys for the application of PEMFCs under harsh conditions. The lattice mismatch generated surface strain and synergic effect between the Pt-rich shell and Co-rich core, which plays a dominant role for enhancing ORR activity. The core-shell structure can lower d-band center of Pt and the adsorption energy of —OH. Furthermore, the Pt-rich shell protected the Co metal from dissolution in acidic conditions.

2.5. PtCo nanowires

Various ultrathin Pt-based nanowires (NWs) have been reported with excellent performance for ORR due to the large percentage of surface atoms with high dispersity and high stability. Hierarchical fcc PtCo NWs with ordered intermetallic structure, Pt rich surface and high-index facets were synthesized using $Co(acac)_3$ and $Pt(acac)_2$ as the precursors by wet-chemical method in the presence of OAm, CTAC and glucose [125]. TEM images revealed that each NW exhibited uneven diameters, Pt-rich surface and crenel-like shape along the entire length (Fig. 5(a)). The growth mechanism study indicated that ultrathin pure Pt nanowires (2 nm) formed within 30 min at the early stage of the synthesis process. The nanowire become uneven, the diameter of which increased from 2 to 5 nm at the reaction time around 1 h, due to the reduction of Co species. Afterward, obvious humps were detected after 3 h due to the further increase of Co content. Around 5 h, typical hierarchical PtCo NWs were obtained. The generation of the hierarchical structure are mainly ascribing to the difference of reduction potentials and diffusions between Pt and Co species. Furthermore, a dependence of the $Co(acac)_3$ amount ascribing to the different reduction/diffusion behavior of Co was observed. The performance of PtCo NWs/C were evaluated for ORR in O_2 saturated 0.1 mol·L^{-1} $HClO_4$ solutions. The MA and SA (3.71 A·mg^{-1}, 7.12 mA·cm^{-2}, Table 1, #20) of the Pt_3Co NWs for ORR are 39.6 and 33.7 folds of the commercial Pt/C catalyst, attributing to the active threefold hollow sites on the Pt-rich (110) and (310) high-index facets. The compressive strain due to smaller atomic size

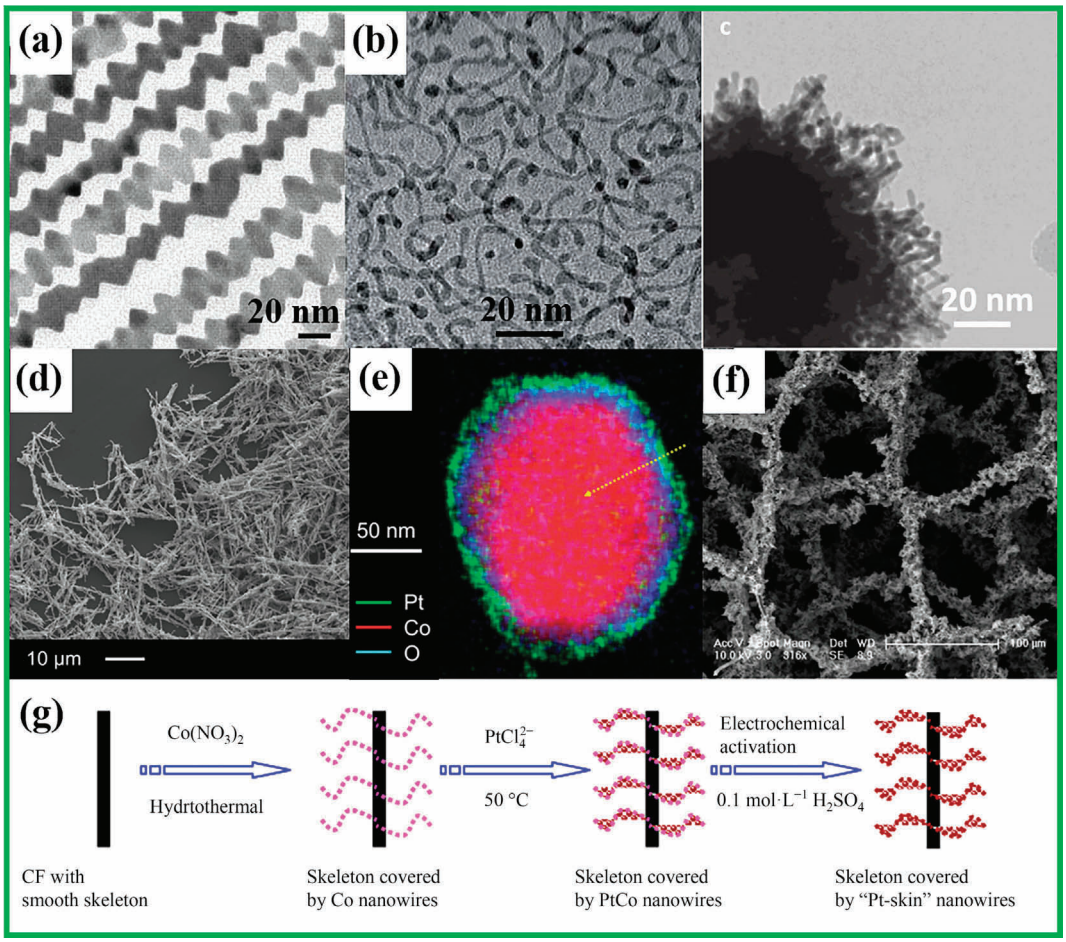

Fig. 5. TEM images of (a) Pt_3Co NWs [125], (b) Pt–Co NWs,[55] (c) PtCo-NW/C [165], (d) FESEM image of PtCo NWs [166], (e) spectrum image of cross-sectioned PtCo NWs [166], (f) SEM images of Co-NWs/CF [126], (g) the fabrication process of PtCo-NWs/CFs [126].

of Co can weaken the oxygen-surface binding, thus improve the ORR performance. Besides, the PtCo NWs were found having better anti-aggregation properties due to high temperature annealing process. The ADT test showed there is 9.1% loss of MA of Pt_3Co NWs/C after 20000 cycles in strong acid solution, which is 31 times higher than that of Pt/C ascribing to the high anti-aggregation properties.

Efficient and stable carbon-supported ultrathin PtCo NWs were produced in OAm and $Cr(CO)_6$, which decomposed into Cr^0/CO and acted as reducing and structure directing agent [55]. TEM image exhibited a uniform nanowire morphology with thin middle part and large ends (diameter about 2 nm, Fig. 5(b)). The MA of PtCo NWs/C catalyst (291.4 $mA{\cdot}mg^{-1}$, Table 1, #21) is 3.4 times higher than commercial Pt/C catalysts (85.5 $mA{\cdot}mg^{-1}$) attributing to the 1D alloy structures with more accessible active crystal facets and untrathin diameter. The improved ORR kinetics are ascribing to the enhanced electron and mass transfer from lattice shrinkage and changed electronic structure. The ADT study showed there is 45.2% decline of MA and 32.5% decline of ECSA after 10000 cycles. The size increasing due to aggregation decreased the number of active sites. Furthermore, the Ostwald ripening and the loss of Co metal in acidic conditions were observed.

Small diameter metallic NWs decorated on carbon nanospheres were obtained by a simple scalable wet chemical synthesis procedure [165]. XRD confirmed that Co has been alloyed into the Pt after annealing process. SEM and TEM showed PtCo/C NWs exhibiting 10–50 nm in length, with diameters of 2–3 nm for the shaft and 4–5 nm for the tip (Fig. 5(c)). PtCo-NW/C showed higher MA than the commercial Pt/C catalyst for ORR. Core-shell NWs (200–300 nm in diameter, Fig. 5(d)–(e)) were obtained by coating Co NWs with Pt by partial galvanic displacement [166]. PtCo NWs exhibited MA and SA (793 $mA{\cdot}mg^{-1}$, 2.78 $mA{\cdot}cm^{-2}$) which are 2.6 and 9.2 times greater than Pt/HSC in 0.1 $mol{\cdot}L^{-1}$ $HClO_4$ solution. Co was selected to avoid migrating through the membrane and plate on the anode. By the same displacement method, Chen's group [126] fabricated PtCo NWs *via* galvanic displacement between $PtCl_4^{2-}$ and Co(0), and then supported on carbon foam network (PtCo-NWs/CF). Ascorbic acid was used as inductive agent to promote the dissolution of Co(0) nanocrystals. TEM and SEM images displayed rough surface and thin carbon framework with average diameters of 88.2 nm and length of 2.93 μm (Fig. 5(f), (g)). The MA of PtCo-NW/CF (2.03 $A{\cdot}mg^{-1}$, Table 1, #22) is 6.3 times higher than the commercial Pt/C (0.32 $A{\cdot}mg^{-1}$) due to the high conductivity and stability of hierarchical porous carbon support. Moreover, the nanowire-like structure can enlarge the surface area and increase the accessible active sites promoting electron migration from O_2 to surface Pt. The stronger O_2 adsorption on Pt surface leads to the fast broken of the O—O bond and thus improved the O_2 reduction efficiency. The kinetics study indicated the first-order reaction towards the concentration of dissolved O_2. The n number calculated to be 4 based on K-L equation, indicating a four-electron oxygen reduction process to H_2O. The ADT was performed in O_2 saturated 0.1 $mol{\cdot}L^{-1}$ KOH. The $E_{1/2}$ and limiting current have almost no shift or decline after 1000 cycles. However, there is more than 20 mV shift of $E_{1/2}$ for the commercial Pt/C cat-

alyst. 1D PtCo mesoporous nanotubes (PtCo MNTs) were obtained by a facile dual-template strategy in aqueous solutions at ambient temperature [89]. The mesoporous PtCo nanotube was formed by galvanic replacement reaction in the presence of Te NWs and F127 as soft template. The SEM image showed that PtCo MNTs has uniform mesopores with pore size of 20 nm on the nanotube wall. The diameter, wall thickness and the mesoporous size of the nanotube decreased with the decreasing of Pt content. The SA of the PtCo MNTs (0.99 mA·cm^{-2}, Table 1, #23) is 4.3 folds of Pt/C (0.23 mA·cm^{-2}), owing to the presence of Co and mesoporous nanotube structure. The large percentage of surface atoms with high dispersity and high stability attributed to the high activity of the PtCo based NWs. Carbon black-supported PtCo NWs (PtCo NWs/C) for PEMFCs were prepared *via* a soft template method [167]. TEM image showed that PtCo NWs retained the nanowire structure after being immobilized on the carbon black support (2.2 nm). The activity of the PtCo NWs/C (125 mA·mg^{-1}, 0.25 mA·cm^{-2}) are 1.5 and 1.6 folds of commercial Pt/C (85 mA·mg^{-1}, 0.16 mA·cm^{-2}). The stability is of PtCo NWs/C is higher than the Pt/C catalyst due to the interconnected NWs network structure. In addition, reduced interatomic Pt—Pt distance of PtCo alloy is favorable for the adsorption of oxygen.

PtCo alloy nanowires with high-index facets showed higher activity. However, the Pt utilization efficiency of the nanowires with large diameter is still relatively low. Paradoxically, the high-index facets vanished gradually under harsh operating conditions if the diameter of the nanowire is too small. Hence, it is interesting but challenging to synthesize nanowires with fewer atomic layers with more exposed surface Pt atoms and lattice contraction.

2.6. PtCo nanoflowers

Highly dispersed flower-like structures $Pt_{69}Co_{31}$ NSNSs (20.3 nm, Fig. 6(a)) assembled by numerous nanosheets were synthesized through a co-reduction solvothermal approach in CTAC, OAm and allantoin [127]. The concentrations of precursors and the allantoin played key role in obtaining the desired nanoflower structure. XPS indicated that Pt^0 and Co^0 are predominant in the sample, which would endow the catalysts with high catalytic activity. The formation mechanism study showed that the variation of the allantoin concentration drove the morphology evolution of the nanoparticles. Around the 4th hour reaction, small nanoparticles (12.5 nm) formed. As the reaction time prolonged to 8 h, clean and distinct sheet-like nanoparticles (19.8 nm) emerged. The diameter of the nanoparticles keeps growing as the reaction time further increased to 12 h and the ill-defined nanodendrites (30.6 nm) were finally obtained. They concluded that the metal complexes are generated by the Van der Waals' force and the electrostatic adsorption between the metal precursor and other reagents. Afterward, the metal complexes were reduced to metallic Pt and Co atoms by the reductants. Pt and Co assembled into PtCo nuclei in the presence of allantoin to decrease the total surface free energy. The PtCo nuclei gathered to form $Pt_{69}Co_{31}$ NSNSs through crystal fusion and orientated growth. The MA and SA (101.93 mA·mg^{-1}, 0.5 mA·cm^{-2}, Table 1, #24) of $Pt_{69}Co_{31}$ NSNSs catalyst are 5.1 and 5 times higher than $Pt_{85}Co_{15}$ NPs (19.96 mA·mg^{-1}, 0.1 mA·cm^{-2}) and PtB (39.73 mA·mg^{-1}, 0.25 mA·cm^{-2}) ascribing to the synergistic effect of PtCo and more accessible active sites. Furthermore, the enlarged ECSA and suffi-

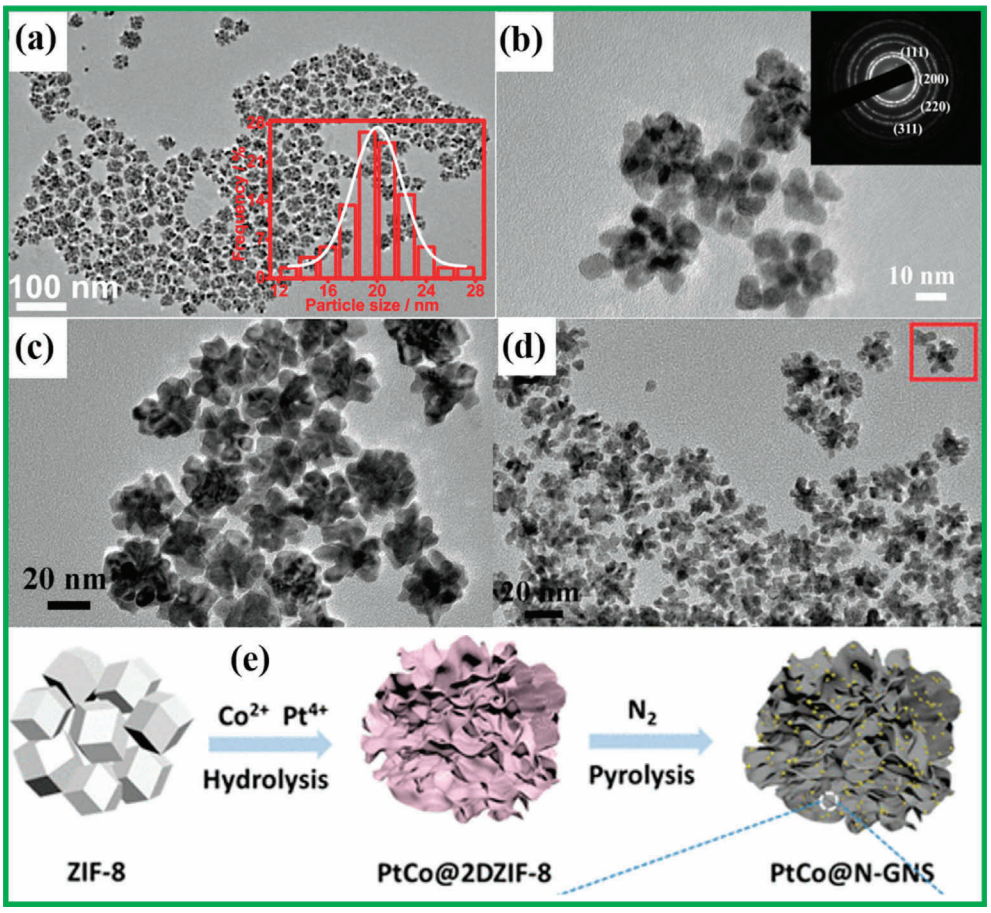

Fig. 6. (a) TEM images and the size distribution of $Pt_{69}Co_{31}$ NSNSs [127]; HRTEM images of (b) $Pt_{71}Co_{29}$ LNFs [53], (c) $Pt_{2.6}Co$ NFs [128]; (d) TEM images of $Pt_{76}Co_{24}$ NMs [45], (e) the synthesis of PtCo@N-GNS [129].

cient surface defects facilitated the oxygen reduction, the mass diffusion, and the electron transport. The ADT study showed there is 40 mV negative shift of have-wave potential of $Pt_{69}Co_{31}$ NSNSs after 1000 cycles, which is smaller than the PtB (42 mV). Alloyed lamellar nanoflowers $Pt_{71}Co_{29}$ LNFs were synthesized using 1-nitroso-2-naphthol and CTAC as co-structure directing agents [53]. Synthesized CTA^+ with long alkyl chain is favorable to disperse the nanocrystals uniformly. TEM images showed that the nanoflowers with particle size around 20 nm were assembled with ultrathin nanoflakes (Fig. 6(b)). The $Pt_{71}Co_{29}$ LNFs displayed 5.6 times higher MA (128.29 $mA{\cdot}mg^{-1}$, Table 1, #25) for ORR than those of commercial PtB (22.91 $mA{\cdot}mg^{-1}$). The ADT study showed there is a 22.3% MA decline of $Pt_{71}Co_{29}$ LNFs and 30.1% decline of PtB catalyst after 1000 cycles in acid solution. Uniform $Pt_{2.6}Co$ nanoflowers were prepared using glucose and CTAC as the reducing and capping agent [128]. TEM showed that the product with highly rough surface contains well-defined flower-like nanostructures (25.44 nm, Fig. 6(c)). The MA of $Pt_{2.6}Co$ NFs (43.97 $mA{\cdot}mg^{-1}$, Table 1, #26) is 1.8 times higher than that of $Pt_{3.7}Co$ NCs and PtB (23.84 $mA{\cdot}mg^{-1}$). The enlarged ECSA, low-coordinated atomic steps and surface defects offered numerous accessible active metal sites, promoted O_2 diffusion and suppressed the Ostwald ripening, thus enhanced the ORR performance. The same group also constructed $Pt_{76}Co_{24}$ nanomyriapods (NMs) using L-glutamic acid to replace the glucose as the green reductant [45]. Myriapod-like structures with particle length around 15.28 nm were obtained as observed by the TEM images (Fig. 6(d)). The MA of $Pt_{76}Co_{24}$ NMs (105.26 $mA{\cdot}mg^{-1}$, Table 1, #27) was 2.2 times higher than the PtB (47.35 $mA{\cdot}mg^{-1}$) for ORR. PtCo nanoalloys supported on N-doped graphene (PtCo@N-GNSs) with hierarchical nanoflower structure were synthesized by hydrolysis and pyrolysis method [129]. ZIF-8 was hydrolyzed with Pt precursors and Co precursors progressively and carbonized to obtain PtCo@N-GNSs (Fig. 6(e)). The formation mechanism study confirmed the major effect of Co species and negligible effect of Pt species on the morphology. The noticed that the sample calcined at 800 °C displayed the highest ORR activity and $E_{1/2}$. The MA of PtCo@N-GNSs is 20.1 times higher than commercial Pt/C for ORR in O_2-saturated 0.1 $mol{\cdot}L^{-1}$ $HClO_4$ solution (Table 1, #28), attributing to the facilitated charge transfer and reduced kinetic energy barrier of the special hierarchy 2D/3D structure. The number of electrons transferred was calculated to be 3.95, implying a four-electron oxygen reduction process. The ADT study showed there is only 10 mV shift of $E_{1/2}$ after 50000 cycles, which is smaller than 35 mV shift of commercial Pt/C catalyst after 20000 cycles. The alloying of PtCo inhibited the Pt oxidation by the oxide-cleansing effect of Co. It is apparently the morphology control is quite a key method to acquire higher electrocatalytic activity and durability. It is essential to explore new methods to synthesize desiring morphologies with superior performance.

3. Support Effect of PtCo Nanoalloy for ORR

For the commercialization of fuel cells, it is extremely important to find a catalyst with both high electrocatalytic activity and long durability. However, metallic nanoparticles present serious dissolution and aggregation. Catalyst supports can effectively disperse nanoparticles and protect them from agglomeration, as well as catalyst dissolution during operation, leading to durable electrochemical activity. Furthermore, the synergistic effect between the support and the metal atom can promote the electron transfers and accelerate the sluggish ORR kinetics ascribing to the lower Fermi level and higher Pt electronic density [168]. The modification of the supports with dopants can improve the catalytic performance for ORR effectively [132]. Hence, it is essential to find a feasible support with high surface area, porous structure and narrow pore size distribution, to increase the electronic conductivity and stabilize the architectures of metallic nanoparticles (Fig. 7), *e.g.* carbon black [169-172], graphene [173,174], carbon nanotube [175–177], N-doped carbon [132,178], and Zeolitic Imidazolate Framework (ZIF) [135,179]. Carbon black has been widely applied for ORR ascribing to the high specific surface area and conductivity. However, the electrooxidation causes activity loss during long-term run. Thus, another candidate supports have been investigated.

3.1. PtCo nanoalloy supported on graphene

As a superior carbon-based nanomaterial, graphene has high mechanical strength, largely available surface area, excellent conductivity, as well as low thermal expansion coefficient [180,181]. Anchoring PtCo-based alloys on graphene can improve the dispersity and endurance of PtCo catalysts due to the presence of carboxyl- and carbonyl-groups on the surface of reduced graphene oxide (rGO), as well as the strong affinity between rGO and PtCo nanoparticles [182]. Wang *et al.* [84] used a facile solvothermal strategy to support sheet-like PtCo nanocrystals on rGO ($Pt_{78}Co_{22}$/rGO) *via* anisotropic and crystal growth in the presence of L-proline and ethylene glycol (EG, Fig. 8(a)). The amino and carboxyl groups on L-Proline can form chelates with the metal salts and decrease the reduction rate [173]. TEM images showed that the sheet-like crystals (10.8 nm) dispersed uniformly on the rGO sheets. The MA of $Pt_{78}Co_{22}$ NCs/rGO (83.64 $mA{\cdot}mg^{-1}$) is 5.8-time higher than PtB (14.30 $mA{\cdot}mg^{-1}$). The electron transfer number they obtained is around 4, indicating a four-electron pathway for ORR. The ADT study showed that there is only 1.1% decline of the current density for $Pt_{78}Co_{22}$ NCs/rGO after 1000 cycles, which is lower than that of Pt/C (9.3%) ascribing to the graphene support. They also studied the methanol tolerance for $Pt_{78}Co_{22}$ NCs/rGO catalyst, little activity loss was observed due to decreased Pt-Co bond energy. Spherical PtCo alloy (3–4 nm, Fig. 8(b)) was immobilized on the surface of single-layer rGO sheets through a facile hydrothermal method using 1,2-hexadecanediol (HAD) as reductant [174]. The MA of PtCo/rGO-HAD (37.4 $mA{\cdot}mg^{-1}$) is slightly higher than PtCo/rGO (32 $mA{\cdot}mg^{-1}$). The presence of HAD promoted the reduction of Co resulting in the further contraction of the lattice. The addition of HAD enhanced the catalytic activity of PtCo/rGO slightly, but displayed a negligible effect on the size and morphology of the PtCo alloy. PtCo concave-nanocubes (CNC, Fig. 8(c)) and concave-polyhedrons (CPH, Fig. 8(d)) bounded by (*hkl*) and (*hk*0) high-index facets were distributed on rGO [130]. They found that one-pot strategy to prepare PtCo/rGO could maximize contact between PtCo nanoparticles and rGO. The SA of the CPH PtCo/rGO (1.53 $mA{\cdot}cm^{-2}$, Table 1, #29) and CNC PtCo/rGO (1.14 $mA{\cdot}cm^{-2}$) are 6.7 and 4.9 folds of the commercial Pt/C (0.23 $mA{\cdot}cm^{-2}$). The CNC PtCo/rGO displayed higher SA than that of supportless CNC PtCo NCs (0.86 $mA{\cdot}cm^{-2}$). The superior performance was attributed to the strong binding between PtCo nanocrystalls and the rGO, which promoted the p-electron polarization and accelerate the electron transfer from rGO to PtCo nanocrystalls.

$Pt_{12}Co$ nanoparticles were deposited on N-doped defective graphene and explored the adsorption energetics, structural features, and electronic properties by the DFT computations (Fig. 8(e)) [183]. N-doped graphene has strong hybridization with the sp^2 dangling bonds at the defect sites, which are anchoring sites for PtCo NPs [183]. The deposited PtCo NPs has lower adsorption ability of the O species, thus higher oxygen reduction reaction kinetics and efficiency, comparing to the freestanding PtCo NPs [183]. Wu *et al.* [85] annealed the Pt nanoparticles supported on nitrogen/metal doped graphene tubes (NGTs, Fig. 8(f)) and obtained PtCoNi/NGT catalyst. Metal/nitrogen co-doped graphene tubes supplied intrin-

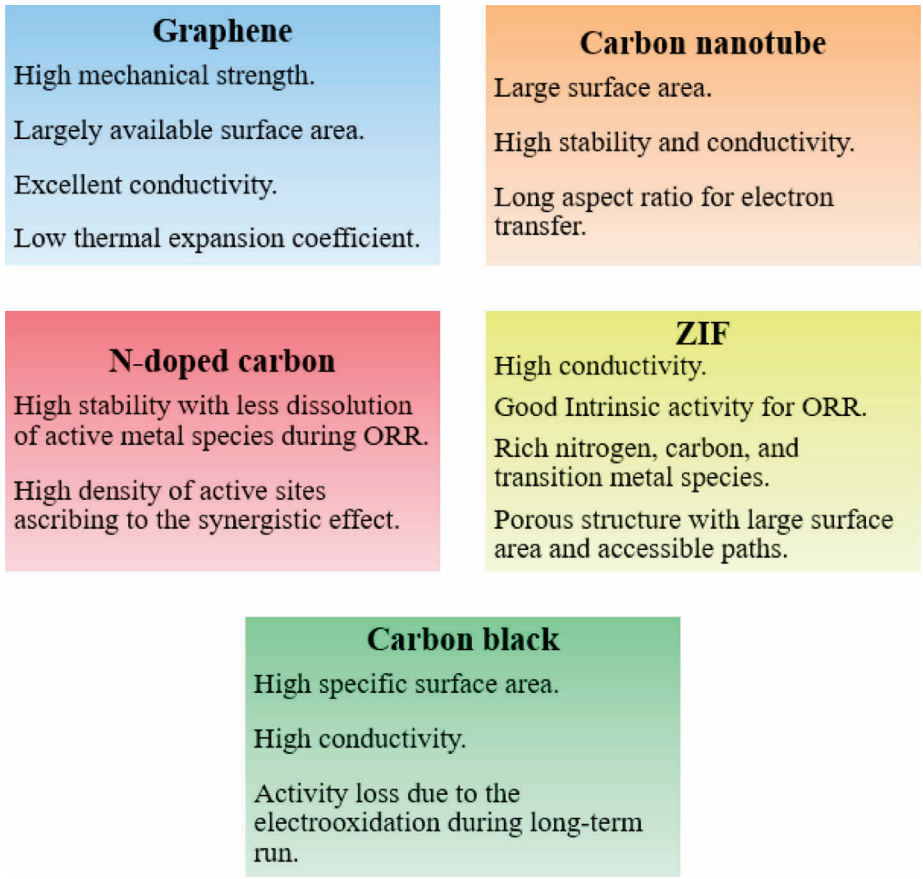

Fig. 7. Supports of PtCo-based nanoalloy for ORR.

sic active sites and appropriate mesopore/macropore distribution which enhanced the mass transfer and the activity of the PtCoNi/NGT catalyst. Furthermore, the synergistic effect between Pt and graphene tubes can prevent carbon corrosion and agglomeration of Pt nanoparticles, leading to higher stability of the Pt based catalysts. PtCo alloy was anchored on citric acid modified graphene to obtain PtCo/CA-G materials (2.2 nm) which showed higher MA and SA (0.48 $mA{\cdot}mg^{-1}$, 0.66 $mA{\cdot}cm^{-2}$, Table 1, #30) than the commercial Pt/C (0.15 $mA{\cdot}mg^{-1}$, 0.24 $mA{\cdot}cm^{-2}$) [131]. The features peaks of *fcc* structure Pt were observed by XRD. The citric acid modification of graphene formed oxygenated functional groups to promote proton transfer without decreasing the electron conductivity or destroying the architecture of graphene. The hydrogen bonding networks connecting with the residual oxygenated functional groups anchor the water molecules in the interlayer of graphene. Furthermore, the interaction of adsorbed water molecules and the functional groups on the surface of graphene form hydrogen bonding networks and generate upstream and downstream fluxes of protons. Thus, the hydrogen-bonding networks generated from the interaction between water molecules and oxygenated groups led to fast proton transfer, thus to high proton conductivity, as depicted by Fig. 9. Hence, the superior performance is ascribed to the higher proton transfer ability and the functional groups of CA-G support.

3.2. PtCo nanoalloy supported on carbon nanotube

Carbon nanotubes (CNTs) are widely used as catalyst supports ascribing to the large surface area, high stability and conductivity, and a long aspect ratio for electron transfer [176]. However, the hydrophobic surface of CNTs usually has many carbonaceous impurities, insufficient binding sites, and thus poor compatibility with metal species [177]. Thus, the surface modification is desired to immobilize more metal nanoparticles. Doping of N or S on the surface can tune the size of the crystal, depress the agglomeration of nanoparticles, and serve as defect sites for nucleation of nanoparticle [177]. Furthermore, S-doped or N-doped CNTs are considered to be more effective than the un-doped ones, ascribing to the various functional groups and higher dispersion of NPs on the tube walls [184]. N-doped CNTs with a "bamboo-like" structure and S-doped CNTs were produced by chemical vapor deposition and annealing treatment (Fig. 8(g),(h)) [175]. Pt_3Co alloy nanocrystals (2 nm) were supported on the as-prepared N-CNTs using ionic liquid as stabilizing agent. The Pt_3Co/N-CNT catalysts showed higher electrocatalytic performance than the Pt_3Co/S-CNT and commercial Pt_3Co/C catalyst due to the nature of the N-CNTs. Pt_3Co/N-CNT has lower quantity of H_2O_2 generated during the oxygen reduction reaction, and higher resistance against the degradation than that of commercial Pt_3Co/CB. PtCo was supported on polyaniline (PAN)-wrapped CNT (PtCo/PAN–CNT, Fig. 8(i)) and evaluated for ORR [176,177]. The increasing of the PAN content on the surface of CNT can improve the catalyst stability, electrode conductivity, hydrophilic property, and the ECSA of the PtCo catalyst. Wei *et al.*[77] constructed a MOF like matrix of bionic catalytic network in which hollow PtCo nanoparticles are anchored on carbon nanotubes (PtCo/CNTs). The HRTEM images displayed that PtCo/CNTs (8 nm) was consisted with interconnected CNTs with various channels for species transporting to the active sites. The activities of the PtCo/CNTs (850 $mA{\cdot}mg^{-1}$, 1.38 $mA{\cdot}cm^{-2}$, Table 1, #31) are 4.8 and 4.3 folds of the commercial Pt/C catalyst, attributing to the hollow structure and the polyhdral MOF-like morphology.

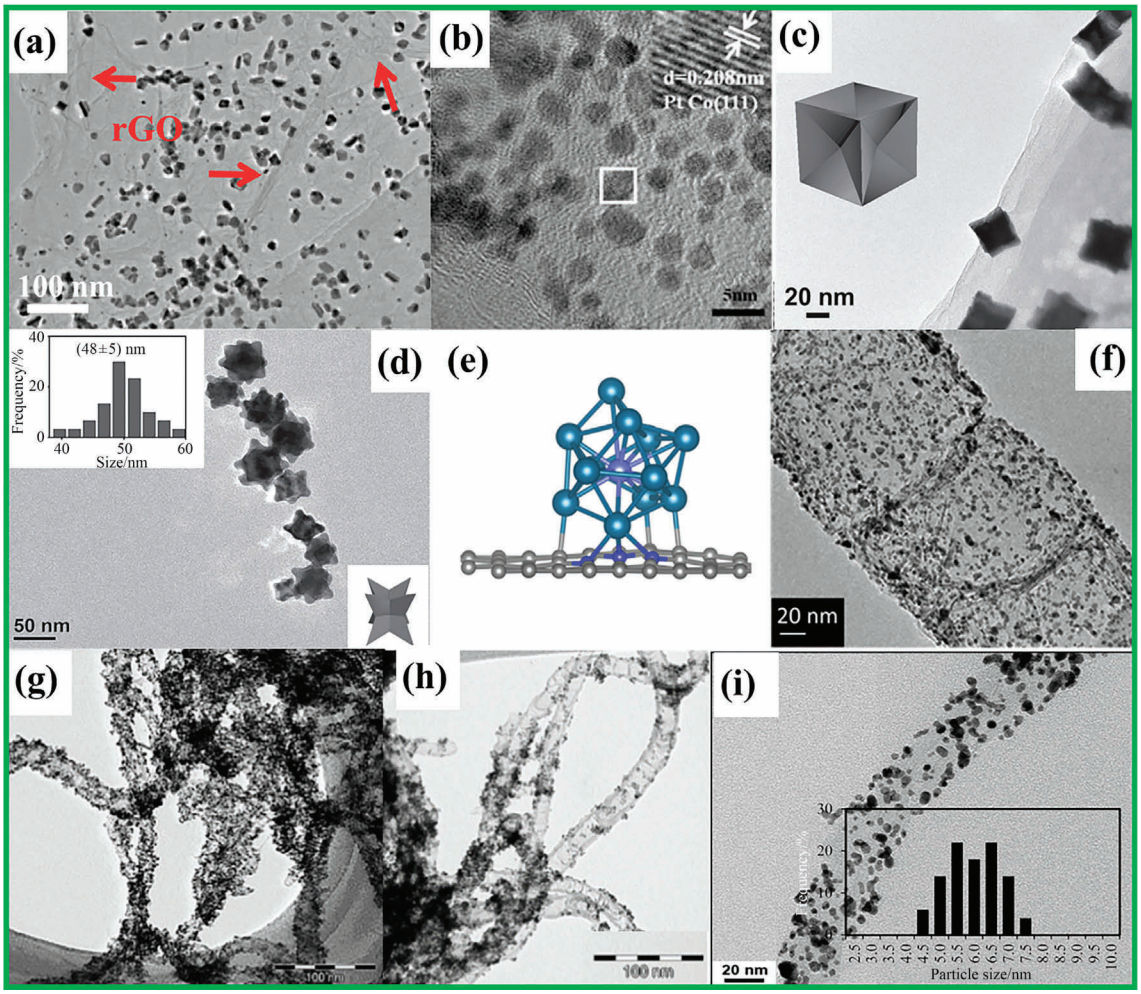

Fig. 8. (a) TEM image of $Pt_{78}Co_{22}$ NCs/rGO [84], (b) HRTEM image of PtCo/rG-O [174], (c) TEM image and structural model of CNC Pt–Co/rGO [130], (d) HRTEM, size distribution and structural model of CPH Pt–Co/rGO [130], (e) the lowest energy structure of configurations of PtCo/N-doped graphene [183], TEM image of (f) Pt CoNi /NGT [85], (g) Pt_3Co/N-CNT [175], (h) Pt_3Co/N-CNTHT [175], (i) PtCo-10PAN-CNT [177].

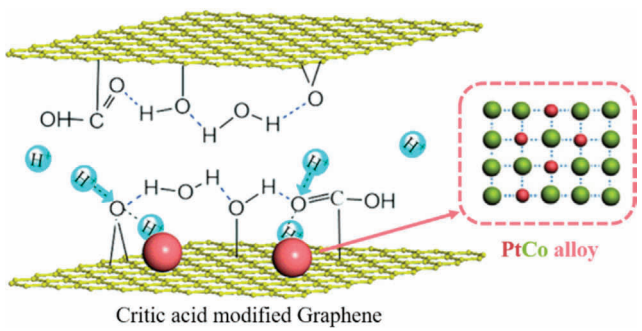

Fig. 9. The protons transfer through the hydrogen-bonding network generated from the interaction between water molecule and oxygenated functional group [131].

3.3. PtCo nanoalloy supported on N-doped carbon

The application of N-doped carbon is an effective strategy to alleviate the coalescence and the dissolution of nanoparticles during the operation of fuel cells under harsh conditions. The N-doped porous carbon supported catalysts exhibited high stability with less detrimental dissolution of the active transition metals from the alloy structure during the fuel cell operation ascribing to the higher affinity of the nitrogen compounds (*e.g.* azide, dopamine) to the metal nanoparticles [132,181]. Furthermore, the synergistic effect between the metal and the N-doped carbon can improve the electron density of the active sites [135]. Chou *et al.* [132] constructed quasi-Pt-allotrope catalyst with hollow Pt_3Co alloy cores and N-doped carbon shell (PtN-C). The STEM-EDS showed the Pt and Co projected distributions in the particles (Fig. 10(a),(b)). XPS spectrum of Co 2p observed that the Co^0, Co^{2+}, and Co^{3+} coexisted which indicated both metallic and oxidized Co presented in the samples. The activity of Pt_3Co@Pt-NC (1200 $mA{\cdot}mg^{-1}$, 2.39 $mA{\cdot}cm^{-2}$, Table 1, #32) are about 8 times higher than the Pt/C (150 $mA{\cdot}mg^{-1}$, 0.3 $mA{\cdot}cm^{-2}$). The holey structure of Pt_3Co@Pt-NC formed internal–external double active layers, exposed abundant active sites, provided accessible tunnels for O_2 and protected these highly active fine nanoparticles from agglomeration. $Co(OH)_2$/CoPt/N-CN catalyst with foam-like morphology has been reported with good activity and durability for ORR [178]. SEM and TEM images showed that PtCo nanocrystals (4.7 nm, Fig. 10(c),(d)) were consisted of a mixed morphologies including flakes, spheres, and sheets. These 3D structures maximized the mass transport and prevented the aggregation, decomposition, and coalescence of the PtCo nanoparticles. The existence of PtCo alloy, $Co(OH)_2$ laminar structure, and the integration of these two, ensured the high ORR activity and stability with super-long cycling life. Chen *et al.* [133] produced PtCo/NHPCC

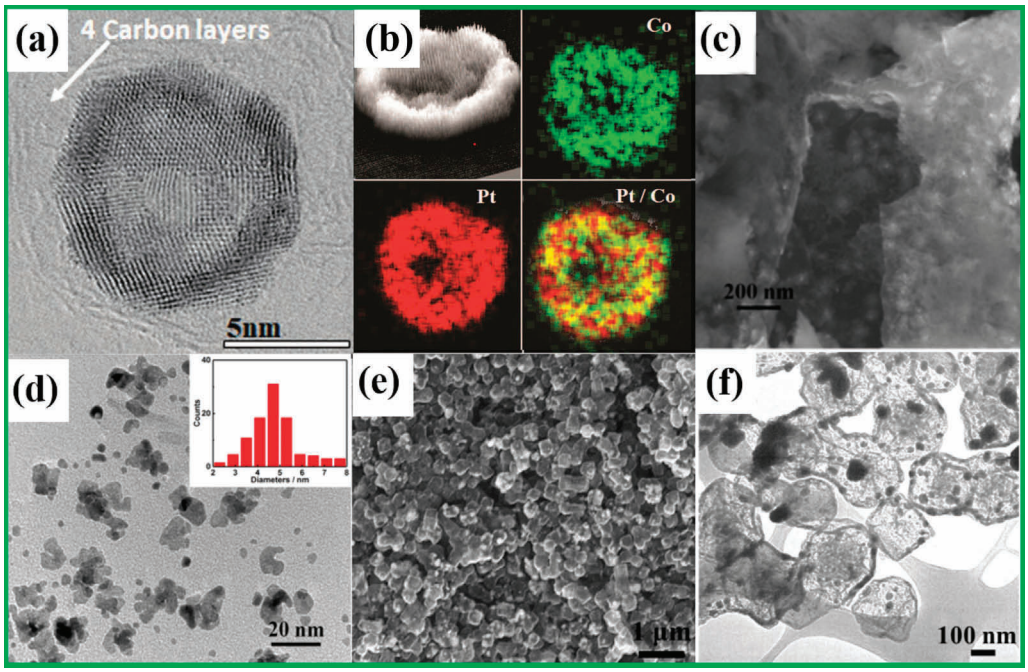

Fig. 10. (a) ABF image and (b) STEM-EDS mapping of H-PtCo@Pt1N-C [132], SEM and TEM images of (c, d) $Co(OH)_2$/CoPt/N-CN [178] and (e, f) PtCo/Co@NHPCC [133].

with Co-based MOFs and immobilized which in N-doped carbon. PtCo/NHPCC has a uniform porous capsule-like morphology consisting of small alloy NPs and large Co nanocrystals. The PtCo/NHPCC demonstrated good activities (570 $mA{\cdot}mg^{-1}$, 0.88 $mA{\cdot}cm^{-2}$, Table 1, #33) which are 5.5 and 4.9 folds of commercial Pt/C (102 $mA{\cdot}mg^{-1}$, 0.18 $mA{\cdot}cm^{-2}$). The superior performance is owing to the small particle size, the N-doping hollow porous carbon capsules with large surface area, and the synergistic effect between metal particles and carbon support. PtCo nanoalloys (Co–N–C/Pt, sub-10 nm) was prepared by introducing Pt and Co precursors in graphene-like N-doped carbon [134]. The as-prepared catalyst showed 1.3 times of SA for ORR (Table 1, #34) than the Pt/C attributing to the synergistic catalytic effect of Co–N_x–C and PtCo nanoalloys. The synergistic effect of PtCo alloy and Co-N_x-C was proposed and depicted in Fig. 11 [134]. For the first step, the oxygen molecule adsorbed on the Co-N_x-C active site with one oxygen atom. The other oxygen atom then anchored on PtCo alloy. The interatomic bond of O_2 broke and accepted proton and electrons (step 2 and step 3). Finally, the final water molecules divorced from the Co-N_x-C and PtCo active sites to complete the four-electron pathway of ORR (step 4) [134].

3.4. PtCo nanoalloy supported on ZIF

ZIF, with imidazole as organic linker with metals, has rich nitrogen, carbon and transition metal [28]. Highly conducting ZIF with large surface area is a potential catalyst support for low temperature fuel cells. The porous structure provided ample paths with large surface area for proton transport and ion exchange, and enable the incorporation of active metals. For ORR, the bonds between nitrogen and metal nanoparticles both served as catalytic active sites [185]. Hence, ZIF can be used as conducting network, supports, precursors, as well as intrinsically active components to catalyze the ORR [136]. Various Co-ZIF–derived catalysts with intensively distributed active sites have been reported highly active for ORR. N-doped carbon-supported PtCo/ZIF (12.7 nm, Fig. 12(a), (b)) synthesizing by thermal decomposition of PtCo-based ZIF displayed 7.9 and 4.4 times higher activity (820 $mA{\cdot}mg^{-1}$, 1.32 $mA{\cdot}cm^{-2}$, Table 1, #35) in acidic media than the Pt/C [135]. The prolong annealing time resulted in a decrease in the thickness of the carbon framework. A highly active electrocatalysts with ultralow Pt composition was reported by Liu's group by using Co- or bimetallic Zn-ZIF as precursors (Fig. 12(c)) [179]. During the thermal treatment of Co-ZIF, Co^{2+} is converted to metallic nanocrystallites and Co-N_x-C_y sites. PtCo nanoparticles dispersed uniformly over Co-N_x-C_y sites forming a core–shell structure (5.6 nm, Fig. 12(d)). PtCo-ZIF achieved higher MA (1770 $mA{\cdot}mg^{-1}$) than that of PtCo (1080 $mA{\cdot}mg^{-1}$) for ORR, attributing to the synergistic effect between PtCo and Co-N_x-C_y sites. Kannan *et al.* [136] synthesized highly active PtCo/ZIF-67 catalyst by pyrolysis of ZIF-67 and Pt precursor. The TEM image of PtCo/ZIF-67 shows the Pt nanoparticles uniformly dispersed on the multi-walled N-CNTs (7–10 nm, Fig. 12(e)). PtCo/ZIF-67 showed the higher limiting current of 5.4 $mA{\cdot}cm^{-2}$ (Table 1, #36) than the Pt/C (4.6 $mA{\cdot}cm^{-2}$) in O_2 saturated electrolyte. Kannan *et al.* [28] reported a bimetallic pyrolyzed NiCo-ZIF supported well-dispersed Pt alloy as shown in the STEM image (3 nm, Fig. 12(f)). XRD showed there are some unalloyed (Ni/Co) particle in PtNiCo/NC sample due to the Ni/Co (111) diffraction. The MA of PtNiCo/NC catalyst (9 $W{\cdot}mg^{-1}$, Table 1, #37) is higher than Pt/C (7.8 $W{\cdot}mg^{-1}$), which is owing to the synergistic impact of N-doped nano-porous carbon and the defect rich surface.

4. Composition Effect of Multi-metallic PtCo-based Nanocatalysts for ORR

A simple and effective method to improve the performance and utilization efficiency of PtCo based-catalyst, various additional transition metals, *e.g.* Ti [186], Ni [139–142,187], Cu [103], Nb [99], Pd [188,189], Mn [106], Sn [98], W [144], La [190], Ir [191–193], Cr [56,194], Au [143,195,196], Ag [102], Al [137], Rh [138], and Fe [41,197,198] are introduced to Pt-based catalytic system aiming to downshift the d-band center by ligand and compressive strain effects, shorten the Pt—Pt bond distance, and change d-band vacancy to further improve the activity and durability of the bimetallic nanoalloy. Jiang *et al.* [137] produced a nanoporous PtCoAl nanoparticles with *in-situ* grown atomic layer Pt skin by a facile alloying/dealloying approach. The activity (2200 $mA{\cdot}mg^{-1}$,

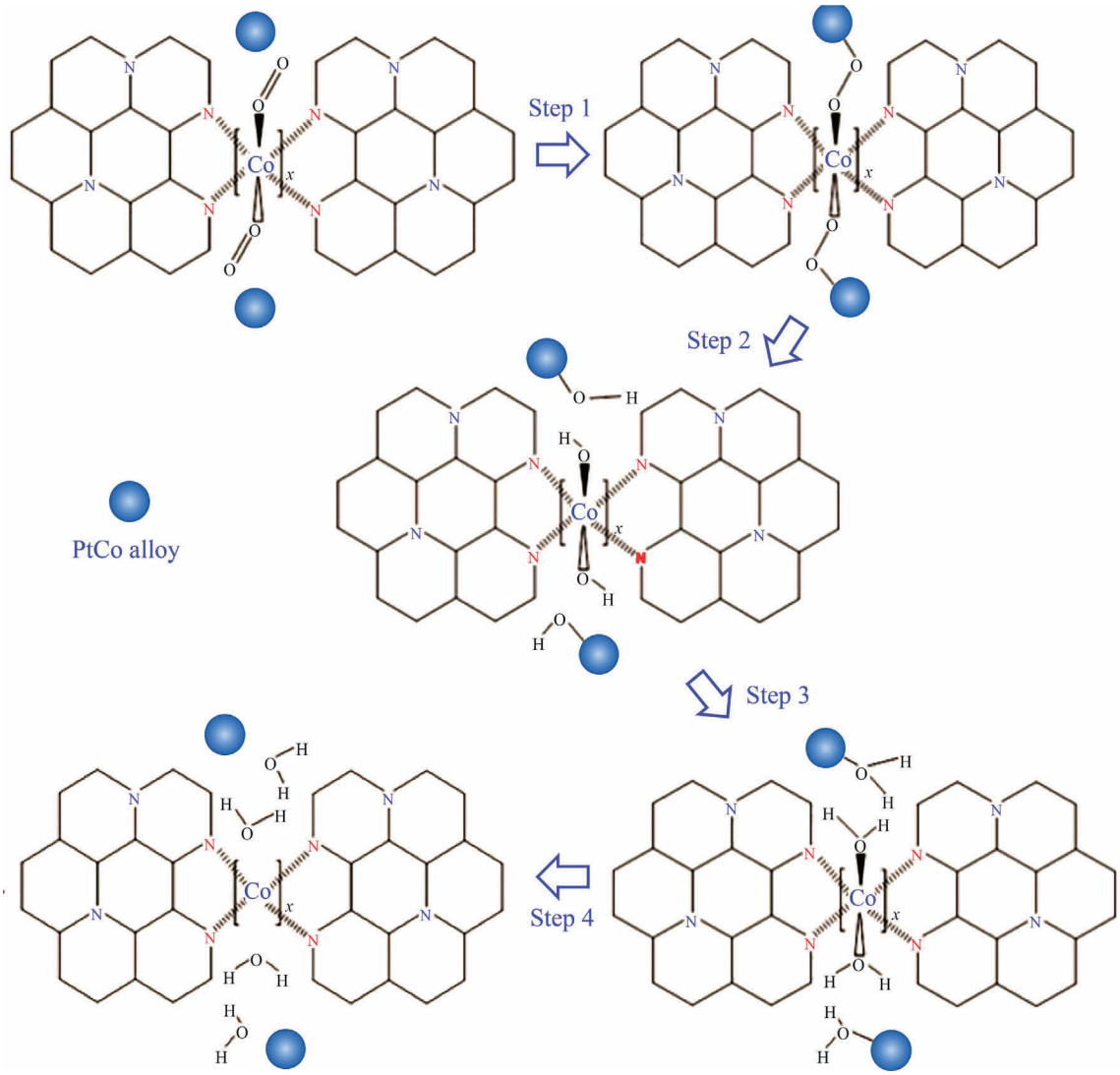

Fig. 11. The proposed synergistic catalytic mechanism of PtCo alloy and Co–N_x–C active sites [134].

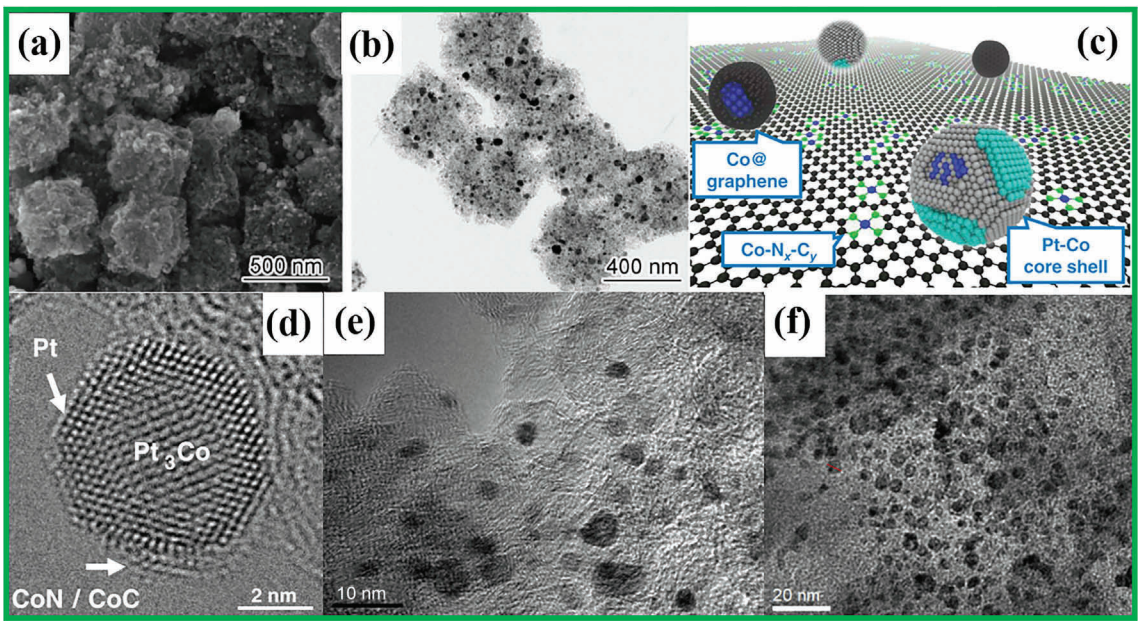

Fig. 12. (a) SEM and (b) TEM images of PtCo@NC-10 [135], (c) LP@PF catalyst structure [179], (d) HRTEM image of Pt-Co alloy NP [179], (e) TEM image of PtCo/ZIF-67 [136], (f) STEM image of PtNiCo [28].

3.40 mA·cm^{-2}, Table 1, #38) of PtCoAl nanocatalyst for the ORR are 20 and 13 folds of the commercial Pt/C, respectively. The compressive strain effect and synergistic ligands due to the strong PtAl and CoAl bonds can weaken the oxygen adsorption energy and suppress the evolution of Pt skin. In the core, the rigid Pt_3Al intermetallic lattice can stabilize Co atoms and thus improve the activity.

Wang *et al.* [138] prepared triple-layered RhCoPt NDs by consecutive reduction of the Rh, Co and Pt precursors in the presence of OAm, CTAC and creatinine. Rh atoms formed initially and acted as seeds to assist the reduction of Co and Pt by regulating the sequential reduction kinetics. TEM image revealed the highly dispersed and uniform dendritic shape with numerous thin branches (60 nm, Fig. 13(a)). The MA of RhCoPt NDs (61.86 mA·mg^{-1}, Table 1, #39) is 1.9, 2.0, and 5.9 folds of Pt/C, PtCo NPs, and PtRh NDs towards ORR.

Fe-based PtCo alloy with Pt-rich surface and abundant high index facets were also prepared by Wang's group by co-reduction of metal salts in formamide [107]. NaI, formamide and CTAB acted as reducing agent, solvent, and capping agent and played vital roles to tune the morphology of nanoparticle. The high proportion of metallic state Pt^0 can raise the number of free Pt sites with enhanced activity. The activities (2590 mA·mg^{-1}, 4.18 mA·cm^{-2}, Table 1, #40) of trimetallic alloy superlattices are 15.2 and 17.4 folds of commercial Pt/C, owing to the ordered structure of PtCoFe which can provide larger surface area, more accessible active sites for the adsorption and activation of small molecules. Mozaffari *et al.* [197] anchored PtCoFe nanoparticles on the S-doped graphene. The presence of SO_3 groups led to stronger adsorption of alloy to the support and increased durability of electrocatalysts. Gan *et al.* [108] prepared ternary PtFeCo alloys and studied the effect of metal compositions. They found that Co can prevent the NPs from sintering and Fe can facilitate the atomic diffusion and thus structural ordering. Moreover, the PtCoFe catalyst exhibited the highest stability and catalytic performance (650 mA·mg^{-1}, Table 1, #41) due to the synergy between Fe and Co, thinner Pt shell and high degree of ordering (Fig. 13(b)). The Pt shell and ordered structure can prevent the etching of non-noble metals and the forming of porous structures. Huh's group synthesized quaternary PtRuFeCo supporting on N-doped graphene [41]. The MA and SA of PtRuFeCo/NG were 0.73 mA·mg^{-1} and 0.80 mA·cm^{-2}, respectively. The presence of additional Ru, Co, and Fe plays important role in adsorbing the OH species, exposed more Pt active sites and decreased the Pt—Pt bond distance.

Li *et al.* [139] prepared ordered $L1_0$-PtNiCo NPs (5 nm, Fig. 13(c)) using a bifunctional Pt/$NiCoO_x$ precursor in the mixture of 1-octadecene, OAm, glucose and PVP. The $L1_0$-$PtNi_{0.8}Co_{0.2}$ catalyst exhibited extremely high activities (2280 mA·mg^{-1}, 4.38 mA·cm^{-2}, Table 1, #42), which are 23 and 19 folds of the commercial Pt/C (100 mA·mg^{-1} and 0.23 mA·cm^{-2}) ascribing to the modified electronic structure and the significantly high crystal ordering structure. DFT calculations suggest that the $L1_0$-$PtNi_{0.8}Co_{0.2}$ core can optimize the Pt—O binding energy and enhance the reaction rate by tuning the surface strain of Pt shell. Hyperbranched dendritic PtNiCo nanoparticles (63–73 nm) with good dispersity and high crystallinity were prepared by a thermal reduction strategy [141]. Sun's group also synthesized $L1_0$-CoNiPt (5 nm) catalysts successfully by organic-phase synthesis followed by annealing and acid-post treatment method to convert the A1 to $L1_0$ structure with a thin Pt shell surface [140]. STEM and EDX images showed core–shell structure of $L1_0$-$Co_1Ni_1Pt_2$ with alternative layers of Pt and Co/Ni, as well as thin (2–4 layers) Pt shell (Fig. 13(d)–(f)). It was observed that $L1_0$ structured can only be obtained by annealing the $Co_1Ni_1Pt_2$, rather than the samples with other compositions, *e.g.,* $Co_1Ni_2Pt_3$ and Ni_1Pt_1. The characterization results indicated $L1_0$-$Co_1Ni_1Pt_2$/C has the largest compression along the (111) direction among all the catalysts prepared. The presence of Pt shell protected the inner core from further dissolution of non-noble metals during the acid treatment. Furthermore, the lattice mismatch between the Pt shell and the $L1_0$ core can generate Pt surface strain. $L1_0$-$Co_1Ni_1Pt_2$/C displayed a MA (3.1 A mg^{-1}) and SA (9.3 mA·cm^{-2}), which is 31 and 58 folds of the commercial Pt/C, respectively (Table 1, #43). After 30000 cycles, there is only 16% drop of MA at 60 °C in 0.1 mol·L^{-1} $HClO_4$. The composition of the used catalyst has no significant change comparing to the fresh catalyst. This good performance is consistent with the theoretical DFT and eigenforce model calculations to predict anisotropic strains levels on distorted (111) Pt surface. $L1_0$-CoNiPt was found has the near-optimum strain levels to provide good performance for ORR due to the anisotropic compressive strain by introducing of Co and Ni metals.

$Pt_3(NiCo)_2$ displayed superior mass and specific activities, which are about 10 and 5 folds to the commercial Pt/C catalyst (Table 1, #44) attributing to the ternary metal composition and the dendritic morphology. Flower-like PtNiCo alloy were obtained by a solvothermal approach followed by annealing process [29]. TEM studies revealed the flower-like structure with approximately eight arms (8 nm) has average diameter of 25 nm (Fig. 13(g)). XRD results observed a reducing of Pt—Pt bond distance due to the formation of alloy nano-structure by introducing additional Co and Ni metals in Pt matrix. The MA and SA (542.7 mA·mg^{-1}, 2.47 mA·cm^{-2}, Table 1, #45) for PtNiCo are 3.5 and 12 folds of Pt/C. Trimetallic PtNiCo nanowires with *fcc* structure displayed a high ECSA of 82.2 m^2 g^{-1} (Fig. 13(h)) [142]. The PtNiCo nanowires demonstrated exceptional mass and specific activities (4200 mA·mg^{-1}, 5.11 mA·cm^{-2}, Table 1, #46) which are 32.3 and 26.9 times higher than those of the commercial Pt/C, respectively. The excellent performance is due to the abundant (111) facets and the Pt-rich shell in the subnanometer PtNiCo nanowires as confirmed by DFT simulations.

Core–shell Pt_3Co@Pd catalysts are prepared and showed good activity for ORR attributing to the optimum oxygen adsorption energies on stable active sites [188]. The DFT calculation indicated that the 3d values of the optimum model catalysts are similar to that of pure Pt (111) and fall around the top of the volcano plot. Wang *et al.* [189] synthesized PtPdCo mesoporous nanoparticles in an aqueous solution in the absence of any organic solvent or hard template. AA is used for the co-reduction of the trimetallic precursors. $Pt_{64.15}Pd_{30.72}Co_{5.13}$ MNs with a highly porous structure (105 nm, Fig. 13(i)) exhibited good activity and stability for ORR due to the synergy of components and structure effects.

Lee *et al.* [143] synthesized an Au-doped PtCo/C catalyst *via* gas-phase reduction and galvanic replacement (Fig. 13(j)). TEM images showed AuPtCo particles with uniform distribution of Au have an average nanoparticle size about 5.6 nm. The current density of the AuPtCo/C (810 mA·mg^{-1}, Table 1, #47) was higher than commercial Pt/C catalysts (230 mA·mg^{-1}). DFT results proved that the presence of Au suppressed the segregation of Co atoms to the surface. Coutanceau *et al.* [195] synthesized spherical $Pt_6Au_2Co_2$ and bean-like $Pt_6Au_2Cu_2$ nanoparticles dispersing on carbon support using a water-in-oil micro-emulsion method for ORR. The $Pt_6Au_2Co_2$ displayed higher activity than the $Pt_6Au_2Cu_2$ due to the spherical structure with higher surface area. Wadayama *et al.* [196] prepared Au-doped PtCo@Pt nanoparticles which has higher stability and SA than the non-Au-doped PtCo nanoparticles. STEM-EDS mapping of the alloy indicated that Au tended to deposit on the corners and edges with low-coordination sites (Fig. 13(k)). Au-PtCo@ Pt showed activity of 5 folds of the commercial Pt/C, but lower activity than the bimetallic PtCo@Pt due to the decrease in the ECSA of Au-PtCo@ Pt. Lee *et al.* [19] synthesized ternary PtCuCo RNFs with reinforced vertex structure by doping Co to the PtCu nanoframes. The reducing power of AA and the Cl^- from

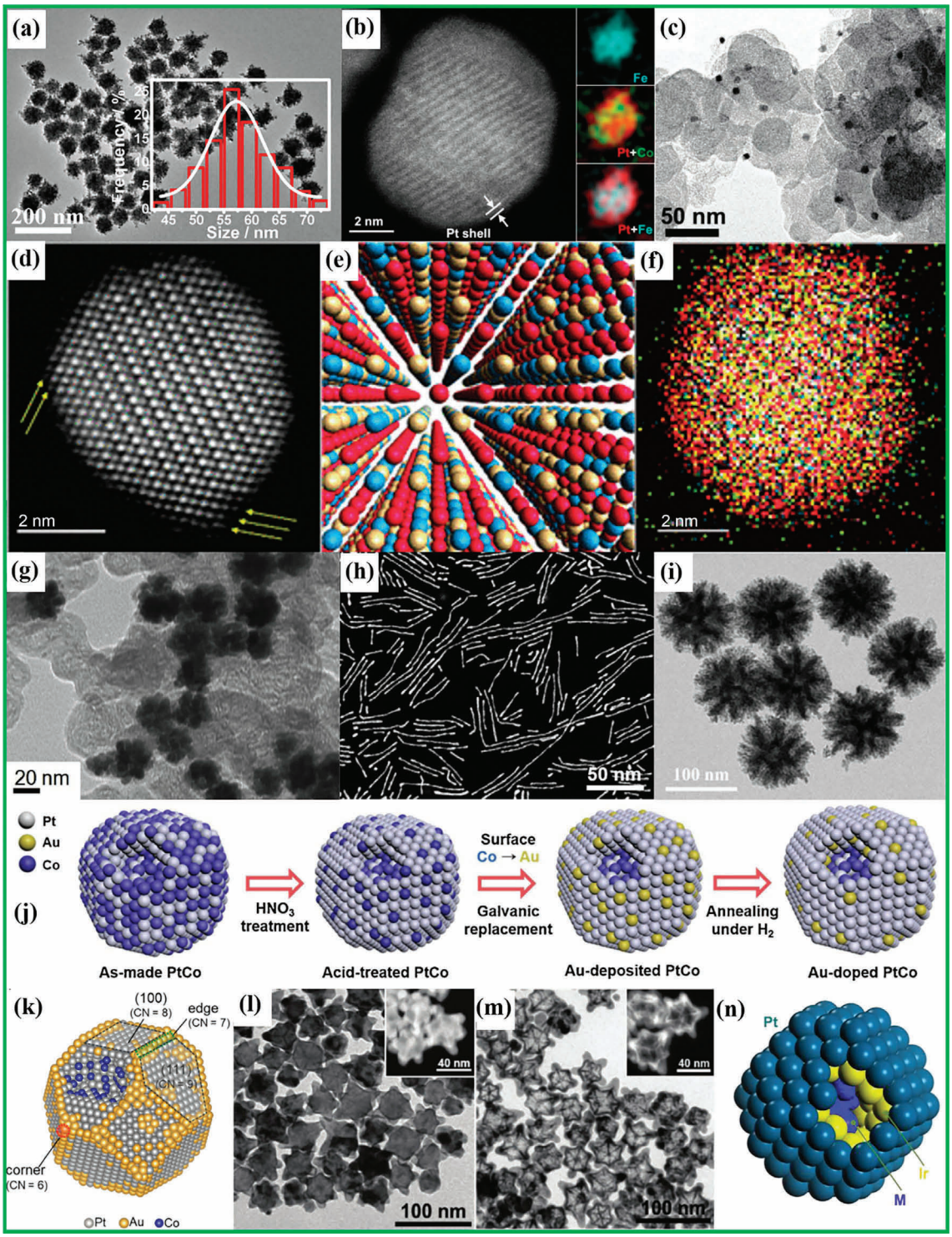

Fig. 13. (a) TEM image and the particle-size distribution of Rh@Co@Pt-skin NDs [138], (b) STEM image of dealloyed PtCoFe-H4 [108], (c) TEM image of C-$L1_0$-$PtNi_{0.8}Co_{0.2}$ NPs [139] and (d) STEM image of a $L1_0$-CoNiPt NP with thin Pt shell [139], (e) a schematic of $L1_0$-CoNiPt and (f) elemental mapping images, where Pt is red, Ni is blue, and Co is yellow [139], (g) PtNiCo-16 h/C [29], (h) STEM image of PtCoNi NWs [142], (i) TEM image of the PtPdCoMNs [189], (j) scheme of the Au-doped PtCo catalyst preparation [43], (k) structural model of the Au-PtCo@Pt NP [196], TEM image of (l) Co-PtCu RNC and (m) Co-PtCu RNF [19], (n) DFT modeling of a PtIrCo model [191].

$CoCl_2$ have significant effect to the generation of rhombic dodecahedral Cu core. The edges of CoPtCu RNC and PtCuCo RNF are around 23.6 and 22.2 nm, respectively, indicating a slight decrease of the particle size after etching process (Fig. 13(l), (m)). The activities of CoPtCu RNF/C (1560 $mA{\cdot}mg^{-1}$, 5.03 $mA{\cdot}cm^{-2}$, Table 1, #48) are superior to those of PtCu RNC/C (770 $mA{\cdot}mg^{-1}$, 2.56 $mA{\cdot}cm^{-2}$) and Pt/C (290 $mA{\cdot}mg^{-1}$, 0.30 $mA{\cdot}cm^{-2}$), attributing to the lower Pt-OH_{ad} binding energy by alloying Co component to Pt surface atoms and the open frame structure.

Tungsten (W), a refractory 5d transition high valency metal, can significantly enhance the electrocatalytic performance of Pt based catalyst for the ORR, ascribing to the unique physical and chemical properties. Graphene-supported ternary PtCoW alloy (2.9 nm) was synthesized by a polyol co-reduction method [144]. The highly

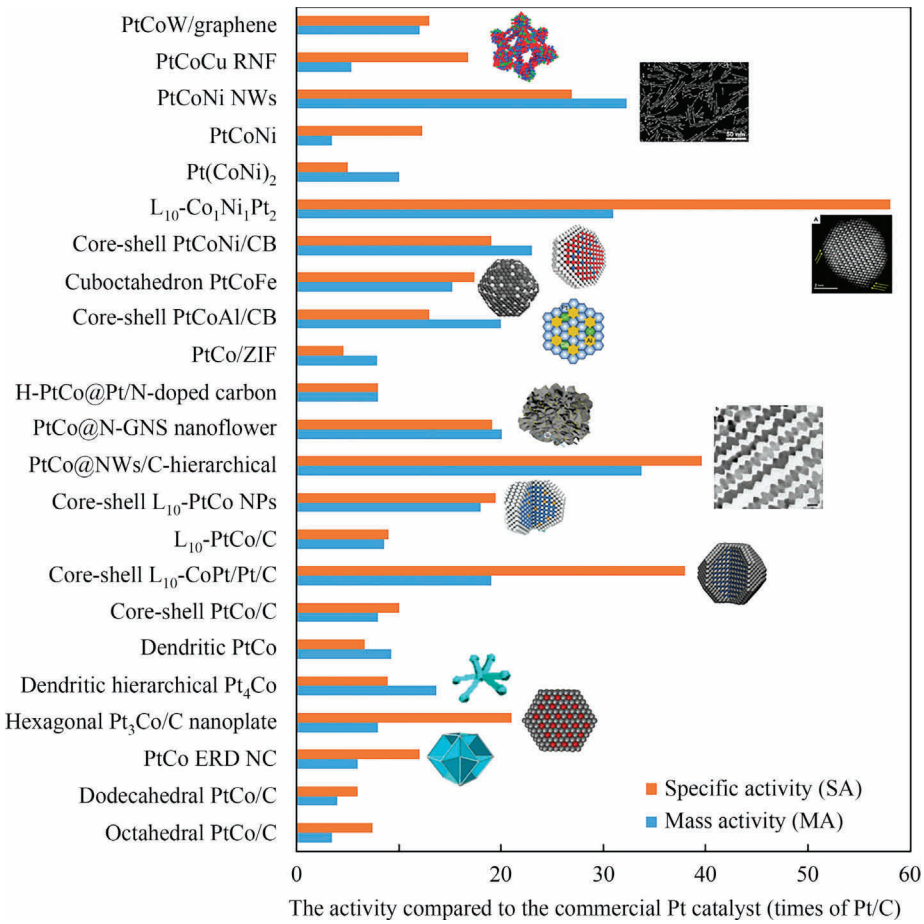

Fig. 14. Summary of the catalytic performance of PtCo catalyst with different morphologies for ORR.

alloyed PtCoW showed superior activities (2250 $mA \cdot mg^{-1}$, 3.41 $mA \cdot cm^{-2}$, Table 1, #49), which are 4.2 and 4.3 folds of PtCo alloy and 12 and 13 folds of Pt/C. The W atoms can strengthen the adsorption of oxygen molecules and facilitate desorption of the oxygenated intermediates on the adjacent Pt active sites, ascribing to the stronger electronegativity, higher unsaturated 5*d* orbitals, and higher valency coordinated with the oxygenated groups. Pastor *et al.* [194] synthesized graphitized carbon supported Pt_2CrCo catalysts *via* the borohydride reduction method. XRD and XPS analysis indicated that Cr_2O_3 and ordered Pt_3Cr alloy formed at higher annealing temperature. The catalyst annealed at 700 °C showed the highest activity, attributing to the shortest Pt—Pt bond distance and the super-lattice planes of the ordered Pt_3Cr alloy. Adzic *et al.* [191] prepared PtIrCo (Fig. 13(n)) and demonstrated higher MA and SA (750 $mA \cdot mg^{-1}$, 0.3 $mA \cdot cm^{-2}$) than that of PtIr catalysts. The PtIrCo synergistic effect changed the electronic/geometric structure and led to segregation effects.

So far, PtNiCo catalyst displayed the best catalytic performance among all the catalysts being reported in the past decades (Fig. 14). The finding is consistent with the volcano plot which was predicted by DFT calculation by Arenz's group [111]. It is reasonably that PtNi and PtCo both located near the apex of the volcano plot.

5. Conclusions

This work summarized the recent progress of the synthesis, morphology and the electrocatalytic performance of PtCo-based multimetallic alloy nanocatalysts for ORR. The synthesis method, size, morphology, and the catalytic performance have been systematically summarized and critically analyzed. The superior activity of PtCo nanoalloys are ascribing to the following factors: (1) Alloying Pt with Co can generate strain and synergetic effect, which can make the down-shift of the Pt d-band center, change the Pt 5d band vacancy, tune the Pt—Pt bond distance, modify the Pt electronic structure, weaken the adsorption of the intermediates to the neighboring Pt atoms, and expose more active sites, thus eventually enhance the catalytic activity, stability, and Pt utilization efficiency. (2) The size, morphology, crystal planes, and surface defects can affect the catalytic activity significantly. The ordered structure NPs have higher stability compared to the disordered ones. The core–shell structure can effectively protect the Co species from dissolution, thus improve the stability of the catalysts. Defect-rich surfaces and high index facets are desired for highly active catalysts for ORR. Larger ECSA can improve the diffusion of the active species and facilitate the electron transport, thus enhance the activity for ORR. (3) The synthesis method and proper operating conditions have significant effect to the morphology of the PtCo based alloys, *e.g.*, the metal precursors, the surfactant, solvent, capping and reducing agent. The preparation temperature and the annealing process also affect the performance significantly. At proper annealing temperature, the disordered PtCo can transform to ordered structure with minimum aggregation. (4) The support has significant effect to the electrocatalytic performance and durability by effectively disperse the active nanoparticles and protect them from collapse and aggregation. Furthermore, the synergistic effect between metal atom and support can accelerate the sluggish ORR kinetics.

For future work, more attentions need to be paid on following aspects: (1) The new strategies to precisely control the size and morphology of the Pt-based alloys are needed to be further inves-

tigate. The reaction parameters, kinds of metal precursors, solvent and reducing/capping/structure directing agents should be regulated. (2) Ternary PtNiCo catalysts displayed the highest MA and SA for ORR comparing to the other catalysts as reviewed and summarized above (Fig. 14). The nature of the adding metal, the metal composition, and the preparation methods should be considered to obtain highly active multimetallic catalysts. (3) Both the activity and stability of the catalysts needs to be considered for the practical application. Hence, new supports with highly porous structures, high conductivity, large ECSA, and good stability are extremely desired. Graphene has great potential as supports for application in fuel cells, however, the massive and inexpensive production of graphene with less defects and impurities needs to be further studied. (4) The utilization efficiency of Pt is still low to make the catalyst more economical. Catalysts with lower proportion of precious Pt metal in alloy, even Pt-free alloy, should be paid more attention, *e.g.*, multi-metallic Pt based nanoalloys, core–shell structure Pt based nanoalloys with Pt skin and non-Pt metal core. Otherwise, non-Pt-based Co catalysts have aroused much attention and made some progress [40], *e.g.*, Co-based N-doped carbon materials (Co-N-C) [199,200], heterometal (Cu, Fe, Ni) co-doped Co-N-C materials [201–204], and nonmetal (S, B, P)-doped Co-N-C materials [205,206]. (5) The reaction and catalyst deactivation mechanism of the ORR process over Pt based nanoalloys should be thoroughly studied by both experimental and DFT calculation methods to understand the structure–activity relationship to the atomic level to guide the rational design of electrocatalyst for ORR. Therefore, more efforts should be devoted to the above-mentioned directions to developing highly active, economic, and durable catalysts for the commercialization of fuel cell systems.

Declaration of Competing Interest

The authors declare that they have no known competing financial interests or personal relationships that could have appeared to influence the work reported in this paper.

Acknowledgements

This study was supported by the National Natural Science Foundation of China (22008262), and Natural Science Foundation of Shandong Province (ZR2020QB187).

References

[1] H. Xu, H.Y. Shang, C. Wang, Y.K. Du, Low-dimensional metallic nanomaterials for advanced electrocatalysis, *Adv. Funct. Mater.* 30 (50) (2020) 2006317.
[2] Z. Li, X.L. Xu, X.H. Lu, C.C. He, J.J. Huang, W. Sun, L. Tian, Synergistic coupling of $FeNi_3$ alloy with graphene carbon dots for advanced oxygen evolution reaction electrocatalysis, *J. Colloid Interface Sci.* 615 (2022) 273–281.
[3] J. Tzadikov, N.R. Levy, L. Abisdris, R. Cohen, M. Weitman, I. Kaminker, A. Goldbourt, Y. Ein-Eli, M. Shalom, Bottom-up synthesis of advanced carbonaceous anode materials containing sulfur for Na-ion batteries, *Adv. Funct. Mater.* 30 (19) (2020) 2000592.
[4] S.J. Yi, H. Jiang, X.J. Bao, S.Q. Zou, J.J. Liao, Z.J. Zhang, Recent progress of Pt-based catalysts for oxygen reduction reaction in preparation strategies and catalytic mechanism, *J. Electroanal. Chem.* 848 (2019) 113279.
[5] C. Biz, M. Fianchini, J. Gracia, Catalysis meets spintronics; spin potentials associated with open-shell orbital configurations enhance the activity of Pt_3Co nanostructures for oxygen reduction: A density functional theory study, *ACS Appl. Nano Mater.* 3 (1) (2020) 506–515.
[6] M. Lokanathan, I.M. Patil, P. Mukherjee, A. Swami, B. Kakade, Molten-salt synthesis of Pt_3Co binary alloy nanoplates as excellent and durable electrocatalysts toward oxygen electroreduction, *ACS Sustainable Chem. Eng.* 8 (2) (2020) 986–993.
[7] H. Xu, Y.T. Zhao, Q. Wang, G.Y. He, H.Q. Chen, Supports promote single-atom catalysts toward advanced electrocatalysis, *Coord. Chem. Rev.* 451 (2022) 214261.
[8] J.K. Nørskov, J. Rossmeisl, A. Logadottir, L. Lindqvist, J.R. Kitchin, T. Bligaard, H. Jónsson, Origin of the overpotential for oxygen reduction at a fuel-cell cathode, *J. Phys. Chem. B* 108 (46) (2004) 17886–17892.
[9] N. Mohan, L. Cindrella, Template-free synthesis of Pt-MO_x (M = Ni, Co & Ce) supported on cubic zeolite-A and their catalytic role in methanol oxidation and oxygen reduction reactions characterized by the hydrodynamic study, *Int. J. Hydrog. Energy* 42 (34) (2017) 21719–21731.
[10] M.H. Shao, Q.W. Chang, J.P. Dodelet, R. Chenitz, Recent advances in electrocatalysts for oxygen reduction reaction, *Chem. Rev.* 116 (6) (2016) 3594–3657.
[11] C. Zalitis, A. Kucernak, X.Q. Lin, J. Sharman, Electrochemical measurement of intrinsic oxygen reduction reaction activity at high current densities as a function of particle size for $Pt_{4-x}Co_x/C$ (x = 0, 1, 3) catalysts, *ACS Catal.* 10 (7) (2020) 4361–4376.
[12] J.H. Lu, L.B. Yang, W. Guo, S.T. Xiao, L.Y. Wang, Y.G. OuYang, P. Gao, The mechanism of Co oxyhydroxide nano-Islands deposited on a Pt surface to promote the oxygen reduction reaction at the cathode of fuel cells, *RSC Adv.* 10 (73) (2020) 44719–44727.
[13] Z. Li, X. Wang, Z. Zhang, J. Hu, Z. Liu, D. Sun, Y. Tang, Concave PtCo nanooctahedra with high-energy 110 facets for the oxygen reduction reaction, *Crystengcomm* 22 (2020) 1541–1546.
[14] Z. Li, W.H. Niu, Z.Z. Yang, N. Zaman, W. Samarakoon, M.Y. Wang, A. Kara, M. Lucero, M.V. Vyas, H. Cao, H. Zhou, G.E. Sterbinsky, Z.X. Feng, Y.G. Du, Y. Yang, Stabilizing atomic Pt with trapped interstitial F in alloyed PtCo nanosheets for high-performance zinc-air batteries, *Energy Environ. Sci.* 13 (3) (2020) 884–895.
[15] J. Wang, J. Zhang, G.G. Liu, C.Y. Ling, B. Chen, J.T. Huang, X.Z. Liu, B. Li, A.L. Wang, Z.N. Hu, M. Zhou, Y. Chen, H.F. Cheng, J.W. Liu, Z.X. Fan, N.L. Yang, C.L. Tan, L. Gu, J.L. Wang, H. Zhang, Crystal phase-controlled growth of PtCu and PtCo alloys on 4H Au nanoribbons for electrocatalytic ethanol oxidation reaction, *Nano Res.* 13 (7) (2020) 1970–1975.
[16] V.S. Men'shchikov, V.E. Guterman, S.V. Belenov, O.A. Spiridonova, D.V. Rezvan, De-alloyed PtCu/C catalysts of methanol electrooxidation, *Russ. J. Electrochem.* 56 (10) (2020) 850–858.
[17] S.V. Belenov, V.S. Men'shchikov, A.Y. Nikulin, N.M. Novikovskii, PtCu/C materials doped with different amounts of gold as the catalysts of oxygen electroreduction and methanol electrooxidation, *Russ. J. Electrochem.* 56 (8) (2020) 660–668.
[18] X.Y. Huang, L.X. You, X.F. Zhang, J.J. Feng, L. Zhang, A.J. Wang, proline assisted solvothermal preparation of Cu-rich rhombic dodecahedral PtCu nanoframes as advanced electrocatalysts for oxygen reduction and hydrogen evolution reactions, *Electrochim. Acta* 299 (2019) 89–97.
[19] T. Kwon, M. Jun, H.Y. Kim, A. Oh, J. Park, H. Baik, S.H. Joo, K. Lee, Vertex-reinforced PtCuCo ternary nanoframes as efficient and stable electrocatalysts for the oxygen reduction reaction and the methanol oxidation reaction, *Adv. Funct. Mater.* 28 (13) (2018) 1706440.
[20] M. Oezaslan, P. Strasser, Activity of dealloyed $PtCo_3$ and $PtCu_3$ nanoparticle electrocatalyst for oxygen reduction reaction in polymer electrolyte membrane fuel cell, *J. Power Sources* 196 (12) (2011) 5240–5249.
[21] Y. Kim, A.A. Jeffery, J. Min, N. Jung, Modulating catalytic activity and durability of PtFe alloy catalysts for oxygen reduction reaction through controlled carbon shell formation, *Nanomaterials (Basel)* 9 (10) (2019) 1491.
[22] D.Y. Chung, S.W. Jun, G. Yoon, S.G. Kwon, D.Y. Shin, P. Seo, J.M. Yoo, H. Shin, Y. H. Chung, H. Kim, B.S. Mun, K.S. Lee, N.S. Lee, S.J. Yoo, D.H. Lim, K. Kang, Y.E. Sung, T. Hyeon, Highly durable and active PtFe nanocatalyst for electrochemical oxygen reduction reaction, *J. Am. Chem. Soc.* 137 (49) (2015) 15478–15485.
[23] B. Arumugam, B.A. Kakade, T. Tamaki, M. Arao, H. Imai, T. Yamaguchi, Enhanced activity and durability for the electroreduction of oxygen at a chemically ordered intermetallic PtFeCo catalyst, *RSC Adv.* 4 (52) (2014) 27510.
[24] D. Schmidt, G.G. Asara, F. Baletto, A kinetic Monte Carlo-blueprint for oxygen reduction on oxide-supported PtNi nanoalloys, *J. Chem. Phys.* 152 (3) (2020) 034107.
[25] I. Khalakhan, L. Vega, M. Vorokhta, T. Skála, F. Viñes, Y.V. Yakovlev, K.M. Neyman, I. Matolínová, Irreversible structural dynamics on the surface of bimetallic PtNi alloy catalyst under alternating oxidizing and reducing environments, *Appl. Catal. B Environ.* 264 (2020) 118476.
[26] X.J. Jia, S. Liu, L. Huang, P. Devaraji, L. Walekar, W. Chen, X.Y. Li, S.H. Liu, L.Q. Mao, $PtNi_xCoy$ concave nanocubes: Synthesis and application in photocatalytic hydrogen generation, *Catal. Sci. Technol.* 10 (1) (2020) 113–123.
[27] Y.J. Sun, Y.J. Li, Y.N. Qin, L. Wang, S.J. Guo, Interfacial engineering in PtNiCo/NiCoS nanowires for enhanced electrocatalysis and electroanalysis, *Chemistry* 26 (18) (2020) 4032–4038.
[28] S. Hanif, X. Shi, N. Iqbal, T. Noor, R. Anwar, A.M. Kannan, ZIF derived PtNiCo/NC cathode catalyst for proton exchange membrane fuel cell, *Appl. Catal. B Environ.* 258 (2019) 117947.
[29] M. Lokanathan, I.M. Patil, B. Kakade, Trimetallic PtNiCo nanoflowers as efficient electrocatalysts towards oxygen reduction reaction, *Int. J. Hydrog. Energy* 43 (18) (2018) 8983–8990.
[30] R. Sriphathoorat, K. Wang, S.P. Luo, M. Tang, H.Y. Du, X.W. Du, P.K. Shen, Well-defined PtNiCo core–shell nanodendrites with enhanced catalytic performance for methanol oxidation, *J. Mater. Chem. A* 4 (46) (2016) 18015–18021.

[31] B.N. Wanjala, R. Loukrakpam, J. Luo, P.N. Njoki, D. Mott, C.J. Zhong, M.H. Shao, L. Protsailo, T. Kawamura, Thermal treatment of PtNiCo electrocatalysts: Effects of nanoscale strain and structure on the activity and stability for the oxygen reduction reaction, *J. Phys. Chem. C* 114 (41) (2010) 17580–17590.

[32] N. Travitsky, T. Ripenbein, D. Golodnitsky, Y. Rosenberg, L. Burshtein, E. Peled, Pt-, PtNi- and PtCo-supported catalysts for oxygen reduction in PEM fuel cells, *J. Power Sources* 161 (2) (2006) 782–789.

[33] Z. Zhao, H.X. Xu, Z.Y. Feng, Y.Q. Zhang, M.S. Cui, D.P. Cao, D.J. Cheng, Design of high-performance Co-based alloy nanocatalysts for the oxygen reduction reaction, *Chem. – A Eur. J.* 26 (18) (2020) 4128–4135.

[34] S. Kobayashi, M. Wakisaka, D.A. Tryk, A. Iiyama, H. Uchida, Effect of alloy composition and crystal face of Pt-skin/$Pt_{100-x}Co_x$ [(111), (100), and (110)] single crystal electrodes on the oxygen reduction reaction activity, *J. Phys. Chem. C* 121 (21) (2017) 11234–11240.

[35] T. Tan, J. Han, J. Deng, Y.M. Kang, M. Yahia, W. Wang, Dealloying co-rich PtPdCo nanoparticles on nitrogen modified carbon as advanced electrocatalyst for ethylene glycol oxidation, *J. Electrochem. Soc.* 167 (4) (2020) 044518.

[36] U. Guevara, R. López, J. Blanco, J. Núñez, Theoretical study of electronic properties and spin density in Pt-Co alloys, *Mater. Res. Express* 6 (9) (2019) 096514.

[37] K. Sato, A. Ito, H. Tomonaga, H. Kanematsu, Y. Wada, H. Asakura, S. Hosokawa, T. Tanaka, T. Toriyama, T. Yamamoto, S. Matsumura, K. Nagaoka, Pt–co alloy nanoparticles on a γ-Al_2O_3 support: The synergistic effect between isolated electron-rich Pt and co for automotive exhaust purification, *ChemPlusChem* 84 (5) (2019) 442.

[38] W.S. Jung, W.H. Lee, H.S. Oh, B.N. Popov, Highly stable and ordered intermetallic PtCo alloy catalyst supported on graphitized carbon containing Co@CN for oxygen reduction reaction, *J. Mater. Chem. A* 8 (38) (2020) 19833–19842.

[39] F.L. Jiang, F.J. Zhu, F. Yang, X.H. Yan, A.M. Wu, L.X. Luo, X.L. Li, J.L. Zhang, Comparative investigation on the activity degradation mechanism of Pt/C and PtCo/C electrocatalysts in PEMFCs during the accelerate degradation process characterized by an *in situ* X-ray absorption fine structure, *ACS Catal.* 10 (1) (2020) 604–612.

[40] Z.Z. Liang, H.Q. Zheng, R. Cao, Recent advances in Co-based electrocatalysts for the oxygen reduction reaction, *Sustain. Energy Fuels* 4 (8) (2020) 3848–3870.

[41] M. Rethinasabapathy, S.M. Kang, Y. Haldorai, N. Jonna, M. Jankiraman, G.W. Lee, S.C. Jang, B. Natesan, C. Roh, Y.S. Huh, Quaternary PtRuFeCo nanoparticles supported N-doped graphene as an efficient bifunctional electrocatalyst for low-temperature fuel cells, *J. Ind. Eng. Chem.* 69 (2019) 285–294.

[42] B. Lim, M. Jiang, P.H. Camargo, E.C. Cho, J. Tao, X. Lu, Y. Zhu, Y. Xia, Pd-Pt bimetallic nanodendrites with high activity for oxygen reduction, *Science* 324 (5932) (2009) 1302–1305.

[43] H. Ataee-Esfahani, L. Wang, Y. Yamauchi, Block copolymer assisted synthesis of bimetallic colloids with Au core and nanodendritic Pt shell, *Chem. Commun. (Camb)* 46 (21) (2010) 3684–3686.

[44] Q.M. Shen, L.P. Jiang, H. Zhang, Q.H. Min, W.H. Hou, J.J. Zhu, Three-dimensional dendritic Pt nanostructures: Sonoelectrochemical synthesis and electrochemical applications, *J. Phys. Chem. C* 112 (42) (2008) 16385–16392.

[45] L.Y. Jiang, X.Y. Huang, A.J. Wang, X.S. Li, J.H. Yuan, J.J. Feng, Facile solvothermal synthesis of $Pt_{76}Co_{24}$ nanomyriapods for efficient electrocatalysis, *J. Mater. Chem. A* 5 (21) (2017) 10554–10560.

[46] J. Kim, W.H. Doh, Y. Kim, K.J. Kim, J.Y. Park, Water-assisted growth of cobalt oxide and cobalt hydroxide overlayers on the $Pt_3Co(111)$ surface, *ACS Appl. Energy Mater.* 2 (12) (2019) 8580–8586.

[47] J. Liu, J.Z. Lan, L.Y. Yang, F. Wang, J. Yin, PtM (M = Fe, co, Ni) bimetallic nanoclusters as active, methanol-tolerant, and stable catalysts toward the oxygen reduction reaction, *ACS Sustainable Chem. Eng.* 7 (7) (2019) 6541–6549.

[48] K. Miyatake, Y. Shimizu, Pt/Co alloy nanoparticles prepared by nanocapsule method exhibit a high oxygen reduction reaction activity in the alkaline media, *ACS Omega* 2 (5) (2017) 2085–2089.

[49] S.Y. Shen, F. Li, L.X. Luo, Y.G. Guo, X.H. Yan, C.C. Ke, J.L. Zhang, DMF-coordination assisted electrodeposition of highly active PtCo alloy catalysts for the oxygen reduction reaction, *J. Electrochem. Soc.* 165 (2) (2018) D43–D49.

[50] B.T. Sneed, D.A. Cullen, R. Mukundan, R.L. Borup, K.L. More, PtCo cathode catalyst morphological and compositional changes after PEM fuel cell accelerated stress testing, *J. Electrochem. Soc.* 165 (6) (2018) F3078–F3084.

[51] Y. Kamitaka, N. Taguchi, Y. Morimoto, Assessing the potential of Co-Pt bronze for electrocatalysis in acidic media, *Catalysts* 8 (7) (2018) 258.

[52] J.N. Zheng, L.L. He, C. Chen, A.J. Wang, K.F. Ma, J.J. Feng, One-pot synthesis of platinum$_3$cobalt nanoflowers with enhanced oxygen reduction and methanol oxidation, *J. Power Sources* 268 (2014) 744–751.

[53] L. Zhang, X.F. Zhang, X.L. Chen, A.J. Wang, D.M. Han, Z.G. Wang, J.J. Feng, Facile solvothermal synthesis of $Pt_{71}Co_{29}$ lamellar nanoflowers as an efficient catalyst for oxygen reduction and methanol oxidation reactions, *J. Colloid Interface Sci.* 536 (2019) 556–562.

[54] D.C. Higgins, S.Y. Ye, S. Knights, Z.W. Chen, Highly durable platinum-cobalt nanowires by microwave irradiation as oxygen reduction catalyst for PEM fuel cell, *Electrochem. Solid-State Lett.* 15 (6) (2012) B83.

[55] Z.K. Liu, Y.H. Yin, D.J. Yang, C.M. Zhang, P.W. Ming, B. Li, S.T. Yang, Efficient synthesis of Pt–Co nanowires as cathode catalysts for proton exchange membrane fuel cells, *RSC Adv.* 10 (11) (2020) 6287–6296.

[56] Q.F. Xiao, M. Cai, M.P. Balogh, M.M. Tessema, Y.F. Lu, Symmetric growth of Pt ultrathin nanowires from dumbbell nuclei for use as oxygen reduction catalysts, *Nano Res.* 5 (3) (2012) 145–151.

[57] S.Q. Hu, Z. Wang, H.L. Chen, S.B. Wang, X.G. Li, X.Y. Zhang, P.K. Shen, Ultrathin PtCo nanorod assemblies with self-optimized surface for oxygen reduction reaction, *J. Electroanal. Chem.* 870 (2020) 114194.

[58] X.L. Chen, L. Zhang, J.J. Feng, W.P. Wang, P.X. Yuan, D.M. Han, A.J. Wang, Facile solvothermal fabrication of polypyrrole sheets supported dendritic platinum-cobalt nanoclusters for highly efficient oxygen reduction and ethylene glycol oxidation, *J. Colloid Interface Sci.* 530 (2018) 394–402.

[59] X.F. Zhang, H.B. Meng, H.Y. Chen, J.J. Feng, K.M. Fang, A.J. Wang, Bimetallic PtCo alloyed nanodendritic assemblies as an advanced efficient and robust electrocatalyst for highly efficient hydrogen evolution and oxygen reduction, *J. Alloys Compd.* 786 (2019) 232–239.

[60] X.X. Zhu, L. Huang, M. Wei, P. Tsiakaras, P.K. Shen, Highly stable Pt-Co nanodendrite in nanoframe with Pt skin structured catalyst for oxygen reduction electrocatalysis, *Appl. Catal. B Environ.* 281 (2021) 119460.

[61] L.H.S. Gasparotto, E.G. Ciapina, E.A. Ticianelli, G. Tremiliosi-Filho, Electrodeposition of PVA-protected PtCo electrocatalysts for the oxygen reduction reaction in H_2SO_4, *J. Power Sources* 197 (2012) 97–101.

[62] O. Sorsa, H. Romar, U. Lassi, T. Kallio, Co-electrodeposited mesoporous PtM (M=Co, Ni, Cu) as an active catalyst for oxygen reduction reaction in a polymer electrolyte membrane fuel cell, *Electrochim. Acta* 230 (2017) 49–57.

[63] M. Vorokhta, I. Khalakhan, M. Vaclavu, G. Kovacs, S.M. Kozlov, P. Kus, T. Skala, N. Tsud, J. Lavkova, V. Potin, I. Matolinova, K.M. Neyman, V. Matolin, Surface composition of magnetron sputtered Pt-Co thin film catalyst for proton exchange membrane fuel cells, *Appl. Surf. Sci.* 365 (2016) 245–251.

[64] S. Kobayashi, M. Aoki, M. Wakisaka, T. Kawamoto, R. Shirasaka, K. Suda, D.A. Tryk, J. Inukai, T. Kondo, H. Uchida, Atomically flat Pt skin and striking enrichment of Co in underlying alloy at Pt_3Co (111) single crystal with unprecedented activity for the oxygen reduction reaction, *ACS Omega* 3 (1) (2018) 154–158.

[65] N. Todoroki, T. Wadayama, Oxygen reduction reaction activity for cobalt-deposited Pt(111) model catalyst surfaces in alkaline solution, *Electrochemistry* 86 (5) (2018) 243–245.

[66] X.M. Zhang, T.W. Gu, S.D. Shi, L.Y. Li, S.S. Yu, Enhanced stability of PtML/MML/WC(0001) multilayer alloys under electrochemical conditions: A first principle study, *ACS Appl. Mater. Interfaces* 10 (18) (2018) 15704–15711.

[67] E. Pizzutilo, J. Knossalla, S. Geiger, J.P. Grote, G. Polymeros, C. Baldizzone, S. Mezzavilla, M. Ledendecker, A. Mingers, S. Cherevko, F. Schüth, K.J.J. Mayrhofer, The space confinement approach using hollow graphitic spheres to unveil activity and stability of Pt-Co nanocatalysts for PEMFC, *Adv. Energy Mater.* 7 (20) (2017) 1700835.

[68] L.K. Wang, Z.H. Tang, W. Yan, Q.N. Wang, H.Y. Yang, S.W. Chen, Co@Pt Core@Shell nanoparticles encapsulated in porous carbon derived from zeolitic imidazolate framework 67 for oxygen electroreduction in alkaline media, *J. Power Sources* 343 (2017) 458–466.

[69] X.J. Wang, W.H. Huang, S.J. Liao, B.T. Li, High oxygen reduction activity of TM_{13}@Pt_{134} and $TM_{12}N$@Pt_{134} (TM=Ti, V, Mn, Fe Co, Ni, and Cu) core-shell electrocatalysts studied by first-principles theory, *Mater. Chem. Phys.* 212 (2018) 378–384.

[70] W.H. Yang, L.L. Zou, Q.H. Huang, Z.Q. Zou, Y.M. Hu, H. Yang, Lattice contracted ordered intermetallic core-shell PtCo@Pt nanoparticles: Synthesis, structure and origin for enhanced oxygen reduction reaction, *J. Electrochem. Soc.* 164 (6) (2017) H331–H337.

[71] S. Dai, Y. You, S. Zhang, W. Cai, M. Xu, L. Xie, R. Wu, G.W. Graham, X. Pan, *In situ* atomic-scale observation of oxygen-driven core-shell formation in Pt_3Co nanoparticles, *Nat. Commun.* 8 (2017) 204.

[72] S. Kaneko, R. Myochi, S. Takahashi, N. Todoroki, T. Wadayama, T. Tanabe, Ultrahigh vacuum synthesis of strain-controlled model Pt(111)-shell layers: Surface strain and oxygen reduction reaction activity, *J. Phys. Chem. Lett.* 8 (21) (2017) 5360–5365.

[73] S.Z. Liu, P. Liu, Optimized Pt-based catalysts for oxygen reduction reaction in alkaline solution: A first principle study, *J. Electrochem. Soc.* 165 (15) (2018) J3090–J3094.

[74] X. Wang, Z.L. Zhao, P. Sun, F.W. Li, One-step synthesis of supported high-index faceted platinum–cobalt nanocatalysts for an enhanced oxygen reduction reaction, *ACS Appl. Energy Mater.* 3 (5) (2020) 5077–5082.

[75] Q.L. Chen, Z.M. Cao, G.F. Du, Q. Kuang, J. Huang, Z.X. Xie, L.S. Zheng, Excavated octahedral Pt-Co alloy nanocrystals built with ultrathin nanosheets as superior multifunctional electrocatalysts for energy conversion applications, *Nano Energy* 39 (2017) 582–589.

[76] G.Z. Hu, E. Gracia-Espino, R. Sandström, T. Sharifi, S.D. Cheng, H.J. Shen, C.Y. Wang, S.J. Guo, G. Yang, T. Wågberg, Atomistic understanding of the origin of high oxygen reduction electrocatalytic activity of cuboctahedral Pt_3Co–Pt core–shell nanoparticles, *Catal. Sci. Technol.* 6 (5) (2016) 1393–1401.

[77] J. Wang, G.P. Wu, W.L. Wang, W.H. Xuan, J.X. Jiang, J.C. Wang, L. Li, W.F. Lin, W. Ding, Z.D. Wei, A neural-network-like catalyst structure for the oxygen reduction reaction: Carbon nanotube bridged hollow PtCo alloy nanoparticles in a MOF-like matrix for energy technologies, *J. Mater. Chem. A* 7 (34) (2019) 19786–19792.

[78] J.R. Li, S. Sharma, X.M. Liu, Y.T. Pan, J.S. Spendelow, M.F. Chi, Y.K. Jia, P. Zhang, D.A. Cullen, Z. Xi, H.H. Lin, Z.Y. Yin, B. Shen, M. Muzzio, C. Yu, Y.S. Kim, A.A. Peterson, K.L. More, S.H. Sun, Hard-magnet $L1_0$-CoPt nanoparticles advance fuel cell catalysis, *Joule* 3 (1) (2019) 124–135.

[79] C. Shen, X.M. Li, Y.J. Wei, Z.M. Cao, H.Q. Li, Y.Q. Jiang, Z.X. Xie, PtCo-excavated rhombic dodecahedral nanocrystals for efficient electrocatalysis, *Nanoscale Adv.* 2 (10) (2020) 4881–4886.

[80] V. di Noto, E. Negro, A. Nale, P.J. Kulesza, I.A. Rutkowska, K. Vezzù, G. Pagot, Correlation between precursor properties and performance in the oxygen reduction reaction of Pt and Co "core-shell" carbon nitride-based electrocatalysts, *Electrocatalysis* 11 (2) (2020) 143–159.

[81] H. Yano, J.M. Song, H. Uchida, M. Watanabe, Temperature dependence of oxygen reduction activity at carbon-supported Pt_XCo (X = 1, 2, and 3) alloy catalysts prepared by the nanocapsule method, *J. Phys. Chem. C* 112 (22) (2008) 8372–8380.

[82] K. Okaya, H. Yano, K. Kakinuma, M. Watanabe, H. Uchida, Temperature dependence of oxygen reduction reaction activity at stabilized Pt skin-PtCo alloy/graphitized carbon black catalysts prepared by a modified nanocapsule method, *ACS Appl. Mater. Interfaces* 4 (12) (2012) 6982–6991.

[83] K. Kakinuma, M. Hayashi, T. Hashimoto, A. Iiyama, M. Uchida, Enhancement of the catalytic activity and load cycle durability of a PtCo alloy cathode catalyst supported on Ta-doped SnO_2 with a unique fused aggregated network microstructure for polymer electrolyte fuel cells, *ACS Appl. Energy Mater.* 3 (7) (2020) 6922–6928.

[84] H.B. Meng, X.F. Zhang, Y.L. Pu, X.L. Chen, J.J. Feng, D.M. Han, A.J. Wang, One-pot solvothermal synthesis of reduced graphene oxide-supported uniform PtCo nanocrystals for efficient and robust electrocatalysis, *J. Colloid Interface Sci.* 543 (2019) 17–24.

[85] M.J. Chen, S. Hwang, J.Z. Li, S. Karakalos, K.T. Chen, Y.H. He, S. Mukherjee, D. Su, G. Wu, Pt alloy nanoparticles decorated on large-size nitrogen-doped graphene tubes for highly stable oxygen-reduction catalysts, *Nanoscale* 10 (36) (2018) 17318–17326.

[86] B. Sravani, P. Raghavendra, Y. Chandrasekhar, Y.V.M. Reddy, R. Sivasubramanian, K. Venkateswarlu, G. Madhavi, L.S. Sarma, Immobilization of platinum-cobalt and platinum-nickel bimetallic nanoparticles on pomegranate peel extract-treated reduced graphene oxide as electrocatalysts for oxygen reduction reaction, *Int. J. Hydrog. Energy* 45 (13) (2020) 7680–7690.

[87] S.M. Alia, K.O. Jensen, B.S. Pivovar, Y.S. Yan, Platinum-coated palladium nanotubes as oxygen reduction reaction electrocatalysts, *ACS Catal.* 2 (5) (2012) 858–863.

[88] S.I. Choi, S.U. Lee, W.Y. Kim, R. Choi, K. Hong, K.M. Nam, S.W. Han, J.T. Park, Composition-controlled PtCo alloy nanocubes with tuned electrocatalytic activity for oxygen reduction, *ACS Appl. Mater. Interfaces* 4 (11) (2012) 6228–6234.

[89] S.L. Yin, Z.Q. Wang, X.Q. Qian, D.D. Yang, Y. Xu, X.N. Li, L. Wang, H.J. Wang, PtM (M = Co, Ni) mesoporous nanotubes as bifunctional electrocatalysts for oxygen reduction and methanol oxidation, *ACS Sustainable Chem. Eng.* 7 (8) (2019) 7960–7968.

[90] S.J. Jiang, Y.W. Ma, G.Q. Jian, H.S. Tao, X.Z. Wang, Y.N. Fan, Y.N. Lu, Z. Hu, Y. Chen, Facile construction of Pt-Co/CN_x nanotube electrocatalysts and their application to the oxygen reduction reaction, *Adv. Mater.* 21 (48) (2009) 4953–4956.

[91] E. Zagoraiou, N. Shroti, M.K. Daletou, Development of Pt-Co catalysts supported on carbon nanotubes using the polyol method—tuning the conditions for optimum properties, *Mater. Today Chem.* 16 (2020) 100263.

[92] M. Lokanathan, I.M. Patil, M. Navaneethan, V. Parey, R. Thapa, B. Kakade, Designing of stable and highly efficient ordered Pt_2CoNi ternary alloy electrocatalyst: The origin of dioxygen reduction activity, *Nano Energy* 43 (2018) 219–227.

[93] M.T. Liu, L.X. Chen, A.J. Wang, K.M. Fang, J.J. Feng, Ternary PtCoNi flower-like networks: One-step additive-free synthesis and highly boosted electrocatalytic performance for hydrogen evolution and oxygen reduction, *Int. J. Hydrog. Energy* 42 (40) (2017) 25277–25284.

[94] R.M. Arán-Ais, F. Dionigi, T. Merzdorf, M. Gocyla, M. Heggen, R.E. Dunin-Borkowski, M. Gliech, J. Solla-Gullón, E. Herrero, J.M. Feliu, P. Strasser, Elemental anisotropic growth and atomic-scale structure of shape-controlled octahedral Pt–Ni–Co alloy nanocatalysts, *Nano Lett.* 15 (11) (2015) 7473–7480.

[95] M. Lokanathan, I.M. Patil, A.K. Usman, A. Swami, P. Walke, M. Navaneethan, B. Kakade, Unusual enhancement in the electroreduction of oxygen by NiCoPt by surface tunability through potential cycling, *RSC Adv.* 7 (19) (2017) 11777–11785.

[96] X.Y. Liu, G.T. Fu, Y. Chen, Y.W. Tang, P.L. She, T.H. Lu, Pt-Pd-Co trimetallic alloy network nanostructures with superior electrocatalytic activity towards the oxygen reduction reaction, *Chem. Eur. J.* 20 (2) (2014) 585–590.

[97] K.C. Wang, H.C. Huang, C.H. Wang, Synthesis of Pd@Pt_3Co/C core–shell structure as catalyst for oxygen reduction reaction in proton exchange membrane fuel cell, *Int. J. Hydrog. Energy* 42 (16) (2017) 11771–11778.

[98] S. Knani, L. Chirchi, W.T. Napporn, S. Baranton, J.M. Léger, A. Ghorbel, Promising ternary Pt-Co-Sn catalyst for the oxygen reduction reaction, *J. Electroanal. Chem.* 738 (2015) 145–153.

[99] S. Matsumoto, M. Nagamine, Z. Noda, J. Matsuda, S.M. Lyth, A. Hayashi, K. Sasaki, PEFC electrocatalysts supported on Nb-SnO_2 for MEAs with high activity and durability: Part II. Application of bimetallic Pt-alloy catalysts, *J. Electrochem. Soc.* 165 (14) (2018) F1164–F1175.

[100] P. Kolla, A. Smirnova, Methanol oxidation and oxygen reduction activity of PtIrCo-alloy nanocatalysts supercritically deposited within 3D carbon aerogel matrix, *Electrochim. Acta* 182 (2015) 20–30.

[101] F. Godínez-Salomón, L. Albiter, R. Mendoza-Cruz, C.P. Rhodes, Bimetallic two-dimensional nanoframes: High activity acidic bifunctional oxygen reduction and evolution electrocatalysts, *ACS Appl. Energy Mater.* 3 (3) (2020) 2404–2421.

[102] P.H. Huang, C.W. Liu, Y.Z. Guo, S.W. Lee, Z.J. Lin, K.W. Wang, The effect of atomic arrangements on the oxygen reduction reaction performance of carbon-supported CoPtAg catalysts, *Electrochim. Acta* 219 (2016) 531–539.

[103] L.B. Zhang, X.D. Ji, X.R. Wang, Y.Q. Fu, H. Zhu, T.X. Liu, Chemically ordered Pt–Co–Cu/C as excellent electrochemical catalyst for oxygen reduction reaction, *J. Electrochem. Soc.* 167 (2) (2020) 024507.

[104] L.M. Guo, D.F. Zhang, L. Guo, Structure design reveals the role of Au for ORR catalytic performance optimization in PtCo-based catalysts, *Adv. Funct. Mater.* 30 (22) (2020) 2001575.

[105] F. Wang, Q. Zhang, Z.Y. Rui, J. Li, J.G. Liu, High-loading Pt-Co/C catalyst with enhanced durability toward the oxygen reduction reaction through surface Au modification, *ACS Appl. Mater. Interfaces* 12 (27) (2020) 30381–30389.

[106] S.C. Liu, S. Li, R.Y. Wang, Y. Rao, Q. Zhong, K. Hong, M. Pan, Preparation of high performance and ultra-low platinum loading membrane electrode assembly for PEMFC commercial application, *J. Electrochem. Soc.* 166 (16) (2019) F1308–F1313.

[107] M.A.Z.G. Sial, H.F. Lin, M. Zulfiqar, S. Ullah, B. Ni, X. Wang, Trimetallic PtCoFe alloy monolayer superlattices as bifunctional oxygen-reduction and ethanol-oxidation electrocatalysts, *Small* 13 (24) (2017) 1700250.

[108] Wang, Yao, Kang, Xia, Gan, Rational development of structurally ordered platinum ternary intermetallic electrocatalysts for oxygen reduction reaction, *Catalysts* 9 (7) (2019) 569.

[109] T. Asset, R. Chattot, M. Fontana, B. Mercier-Guyon, N. Job, L. Dubau, F. Maillard, Cover feature: A review on recent developments and prospects for the oxygen reduction reaction on hollow Pt-alloy nanoparticles, *ChemPhysChem* 19 (13) (2018) 1552–1567.

[110] J. Stacy, Y.N. Regmi, B. Leonard, M.H. Fan, The recent progress and future of oxygen reduction reaction catalysis: A review, *Renew. Sustain. Energy Rev.* 69 (2017) 401–414.

[111] G.W. Sievers, A.W. Jensen, J. Quinson, A. Zana, F. Bizzotto, M. Oezaslan, A. Dworzak, J.J.K. Kirkensgaard, T.E.L. Smitshuysen, S. Kadkhodazadeh, M. Juelsholt, K.M.Ø. Jensen, K. Anklam, H. Wan, J. Schäfer, K. Čépe, M. Escudero-Escribano, J. Rossmeisl, A. Quade, V. Brüser, M. Arenz, Self-supported Pt–CoO networks combining high specific activity with high surface area for oxygen reduction, *Nat. Mater.* 20 (2) (2021) 208–213.

[112] T.N. Tran, H.Y. Lee, J.D. Park, T.H. Kang, B.J. Lee, J.S. Yu, Synergistic CoN-decorated Pt catalyst on two-dimensional porous Co–N-doped carbon nanosheet for enhanced oxygen reduction activity and durability, *ACS Appl. Energy Mater.* 3 (7) (2020) 6310–6322.

[113] V. Stamenkovic, B.S. Mun, K.J. Mayrhofer, P.N. Ross, N.M. Markovic, J. Rossmeisl, J. Greeley, J.K. Nørskov, Changing the activity of electrocatalysts for oxygen reduction by tuning the surface electronic structure, *Angew. Chem. Int. Ed Engl.* 45 (18) (2006) 2897–2901.

[114] Y.X. Ma, L.S. Yin, T. Yang, Q.L. Huang, M.S. He, H. Zhao, D.E. Zhang, M.Y. Wang, Z.W. Tong, One-pot synthesis of concave platinum-cobalt nanocrystals and their superior catalytic performances for methanol electrochemical oxidation and oxygen electrochemical reduction, *ACS Appl. Mater. Interfaces* 9 (41) (2017) 36164–36172.

[115] S.P. Chen, M.F. Li, M.Y. Gao, J.B. Jin, M.A. van Spronsen, M.B. Salmeron, P.D. Yang, High-performance Pt–Co nanoframes for fuel-cell electrocatalysis, *Nano Lett.* 20 (3) (2020) 1974–1979.

[116] L.Y. Jiang, A.J. Wang, X.S. Li, J.H. Yuan, J.J. Feng, Facile solvothermal synthesis of Pt_4Co multi-dendrites: An effective electrocatalyst for oxygen reduction and glycerol oxidation, *ChemElectroChem* 4 (11) (2017) 2909–2914.

[117] K. Eid, H.J. Wang, V. Malgras, S.M. Alshehri, T. Ahamad, Y. Yamauchi, L. Wang, One-step solution-phase synthesis of bimetallic PtCo nanodendrites with high electrocatalytic activity for oxygen reduction reaction, *J. Electroanal. Chem.* 779 (2016) 250–255.

[118] Y.Z. Cai, P. Gao, F.H. Wang, H. Zhu, Carbon supported chemically ordered nanoparicles with stable Pt shell and their superior catalysis toward the oxygen reduction reaction, *Electrochim. Acta* 245 (2017) 924–933.

[119] Y.S. Kang, D. Choi, H.Y. Park, S.J. Yoo, Tuning the surface structure of PtCo nanocatalysts with high activity and stability toward oxygen reduction, *J. Ind. Eng. Chem.* 78 (2019) 448–454.

[120] S. Lee, J.H. Jang, I. Jang, D. Choi, K.S. Lee, D. Ahn, Y.S. Kang, H.Y. Park, S.J. Yoo, Development of robust Pt shell through organic hydride donor in PtCo@Pt core-shell electrocatalysts for highly stable proton exchange membrane fuel cells, *J. Catal.* 379 (2019) 112–120.

[121] L. Wang, W.P. Gao, Z.Y. Liu, Z.H. Zeng, Y.F. Liu, M. Giroux, M.F. Chi, G.F. Wang, J. Greeley, X.Q. Pan, C. Wang, Core–shell nanostructured cobalt–platinum electrocatalysts with enhanced durability, *ACS Catal.* 8 (1) (2018) 35–42.

[122] T. Xiang, L. Fang, J. Wan, L. Liu, J.J. Gao, H.T. Xu, H.J. Zhang, X. Gu, Y. Wang, Thickness-tunable core–shell Co@Pt nanoparticles encapsulated in sandwich-like carbon sheets as an enhanced electrocatalyst for the oxygen reduction reaction, *J. Mater. Chem. A* 6 (43) (2018) 21396–21403.

[123] J.D. Lee, D. Jishkariani, Y.R. Zhao, S. Najmr, D. Rosen, J.M. Kikkawa, E.A. Stach, C.B. Murray, Tuning the electrocatalytic oxygen reduction reaction activity of Pt–Co nanocrystals by cobalt concentration with atomic-scale understanding, *ACS Appl. Mater. Interfaces* 11 (30) (2019) 26789–26797.

[124] J.S. Liang, N. Li, Z.L. Zhao, L. Ma, X.M. Wang, S.Z. Li, X. Liu, T.Y. Wang, Y.P. Du, G. Lu, J.T. Han, Y.H. Huang, D. Su, Q. Li, Tungsten-doped $L1_0$-PtCo ultrasmall

nanoparticles as a high-performance fuel cell cathode, *Angew. Chem. Int. Ed.* 58 (43) (2019) 15471–15477.
[125] L.Z. Bu, S.J. Guo, X. Zhang, X. Shen, D. Su, G. Lu, X. Zhu, J.L. Yao, J. Guo, X.Q. Huang, Surface engineering of hierarchical platinum-cobalt nanowires for efficient electrocatalysis, *Nat. Commun.* 7 (2016) 11850.
[126] M.M. Liu, S.J. He, W. Chen, Free-standing 3D hierarchical carbon foam-supported PtCo nanowires with "Pt skin" as advanced electrocatalysts, *Electrochim. Acta* 199 (2016) 218–226.
[127] Z.-N. Yu, Z. Zhang, Z.-S. Lv, M.-T. Liu, L. Zhang, A.-J. Wang, L.-Y. Jiang, J.-J. Feng, $Platinum_{69}$-$cobalt_{31}$ alloyed nanosheet nanoassemblies as advanced bifunctional electrocatalysts for boosting ethylene glycol oxidation and oxygen reduction, *J. Colloid Interface Sci.* 525 (2018) 216–224.
[128] L.Y. Jiang, X.X. Lin, A.J. Wang, J.H. Yuan, J.J. Feng, X.S. Li, Facile solvothermal synthesis of monodisperse $Pt_{2.6}Co_1$ nanoflowers with enhanced electrocatalytic activity towards oxygen reduction and hydrogen evolution reactions, *Electrochim. Acta* 225 (2017) 525–532.
[129] J.J. Gao, F. Zhang, W. Gan, Y.W. Gui, H.J. Qiu, H.L. Li, Q.H. Yuan, MOF-derived 2D/3D hierarchical N-doped graphene as support for advanced Pt utilization in ethanol fuel cell, *ACS Appl. Mater. Interfaces* 12 (42) (2020) 47667–47676.
[130] Y.C. Qin, X. Zhang, X.P. Dai, H. Sun, Y. Yang, X.S. Li, Q.X. Shi, D.W. Gao, H. Wang, N.F. Yu, S.G. Sun, Graphene oxide-assisted synthesis of Pt-Co alloy nanocrystals with high-index facets and enhanced electrocatalytic properties, *Small* 12 (4) (2016) 524–533.
[131] Y.G. Zhao, J.J. Liu, Y.J. Wu, F. Wang, Proton conductive Pt-Co nanoparticles anchoring on citric acid functionalized graphene for efficient oxygen reduction reaction, *J. Power Sources* 360 (2017) 528–537.
[132] W.H. Lai, B.W. Zhang, Z.P. Hu, X.M. Qu, Y.X. Jiang, Y.X. Wang, J.Z. Wang, H.K. Liu, S.L. Chou, The quasi-Pt-allotrope catalyst: Hollow PtCo@single-atom Pt_1 on nitrogen-doped carbon toward superior oxygen reduction, *Adv. Funct. Mater.* 29 (13) (2019) 1807340.
[133] J. Ying, J. Li, G.P. Jiang, Z.P. Cano, Z. Ma, C. Zhong, D. Su, Z.W. Chen, Metal-organic frameworks derived platinum-cobalt bimetallic nanoparticles in nitrogen-doped hollow porous carbon capsules as a highly active and durable catalyst for oxygen reduction reaction, *Appl. Catal. B Environ.* 225 (2018) 496–503.
[134] C. Cao, L.L. Wei, Q.R. Zhai, J.L. Ci, W.W. Li, G. Wang, J.Q. Shen, Gas-flow tailoring fabrication of graphene-like Co-N_x-C nanosheet supported sub-10 nm PtCo nanoalloys as synergistic catalyst for air-cathode microbial fuel cells, *ACS Appl. Mater. Interfaces* 9 (27) (2017) 22465–22475.
[135] N.N. Du, C.M. Wang, R. Long, Y.J. Xiong, N-doped carbon-stabilized PtCo nanoparticles derived from Pt@ZIF-67: Highly active and durable catalysts for oxygen reduction reaction, *Nano Res.* 10 (9) (2017) 3228–3237.
[136] X. Shi, N. Iqbal, S.S. Kunwar, G. Wahab, H.A. Kasat, A.M. Kannan, PtCo@NCNTs cathode catalyst using ZIF-67 for proton exchange membrane fuel cell, *Int. J. Hydrog. Energy* 43 (6) (2018) 3520–3526.
[137] R.-Q. Yao, L.-P. Han, X.-Y. Lang, T. Cheng, Z. Wen, G. Liu, Q. Jiang, Nanoporous $(Pt_{1-x}Co_x)$(3)Al intermetallic compound as a high-performance catalyst for oxygen reduction reaction, *Int. J. Hydrogen Energy* 43 (2018) 19947–19954.
[138] X.-Y. Wang, J.-J. Feng, L. Zhang, X. Luo, Q.-L. Zhang, A.-J. Wang, Bioinspired one-pot fabrication of triple-layered Rh@Co@Pt-skin core-shell nanodendrites: A highly active and durable electrocatalyst towards oxygen reduction reaction, *Electrochim. Acta* 321 (2019) 134660.
[139] T.Y. Wang, J.S. Liang, Z.L. Zhao, S.Z. Li, G. Lu, Z.C. Xia, C. Wang, J.H. Luo, J.T. Han, C. Ma, Y.H. Huang, Q. Li, Sub-6 nm fully ordered $L1_0$-Pt–Ni–Co nanoparticles enhance oxygen reduction *via* co doping induced ferromagnetism enhancement and optimized surface strain, *Adv. Energy Mater.* 9 (17) (2019) 1803771.
[140] J.R. Li, S. Sharma, K.C. Wei, Z.T. Chen, D. Morris, H.H. Lin, C. Zeng, M.F. Chi, Z.Y. Yin, M. Muzzio, M.Q. Shen, P. Zhang, A.A. Peterson, S.H. Sun, Anisotropic strain tuning of $L1_0$ ternary nanoparticles for oxygen reduction, *J. Am. Chem. Soc.* 142 (45) (2020) 19209–19216.
[141] G.M. Leteba, D.R.G. Mitchell, P.B.J. Levecque, C.I. Lang, Solution-grown dendritic Pt-based ternary nanostructures for enhanced oxygen reduction reaction functionality, *Nanomaterials (Basel)* 8 (7) (2018) 462.
[142] K.Z. Jiang, D.D. Zhao, S.J. Guo, X. Zhang, X. Zhu, J. Guo, G. Lu, X.Q. Huang, Efficient oxygen reduction catalysis by subnanometer Pt alloy nanowires, *Sci. Adv.* 3 (2) (2017) e1601705.
[143] J. Choi, J. Cho, C.W. Roh, B.S. Kim, M.S. Choi, H. Jeong, H.C. Ham, H. Lee, Au-doped PtCo/C catalyst preventing Co leaching for proton exchange membrane fuel cells, *Appl. Catal. B Environ.* 247 (2019) 142–149.
[144] Y.J. Wu, Y.G. Zhao, J.J. Liu, F. Wang, Adding refractory 5d transition metal W into PtCo system: An advanced ternary alloy for efficient oxygen reduction reaction, *J. Mater. Chem. A* 6 (23) (2018) 10700–10709.
[145] S.H. Noh, M.H. Seo, J.K. Seo, P. Fischer, B. Han, First principles computational study on the electrochemical stability of Pt–Co nanocatalysts, *Nanoscale* 5 (18) (2013) 8625.
[146] N.K. Chaudhari, J. Joo, H.B. Kwon, B. Kim, H.Y. Kim, S.H. Joo, K. Lee, Nanodendrites of platinum-group metals for electrocatalytic applications, *Nano Res.* 11 (12) (2018) 6111–6140.
[147] C.Y. Zhai, H.M. Zhang, J.Y. Hu, L.X. Zeng, M.Q. Xue, Y.K. Du, M.S. Zhu, Enhanced formic acid electrooxidation reaction enabled by 3D PtCo nanodendrites electrocatalyst, *J. Alloys Compd.* 774 (2019) 274–281.
[148] H.P. Rong, J.J. Mao, P.Y. Xin, D.S. He, Y.J. Chen, D.S. Wang, Z.Q. Niu, Y.E. Wu, Y. D. Li, Kinetically controlling surface structure to construct defect-rich intermetallic nanocrystals: Effective and stable catalysts, *Adv. Mater.* 28 (13) (2016) 2540–2546.
[149] W.S. Jung, B.N. Popov, Effect of pretreatment on durability of fct-structured Pt-based alloy catalyst for the oxygen reduction reaction under operating conditions in polymer electrolyte membrane fuel cells, *ACS Sustain. Chem. Eng.* 5 (11) (2017) 9809–9817.
[150] Y. Xiong, Y. Yang, F.J. DiSalvo, H.D. Abruña, Synergistic bimetallic metallic organic framework-derived Pt-Co oxygen reduction electrocatalysts, *ACS Nano* 14 (10) (2020) 13069–13080.
[151] Y.H. Wang, J.B. Le, W.Q. Li, J. Wei, P.M. Radjenovic, H. Zhang, X.S. Zhou, J. Cheng, Z.Q. Tian, J.F. Li, *In situ* spectroscopic insight into the origin of the enhanced performance of bimetallic nanocatalysts towards the oxygen reduction reaction (ORR), *Angew. Chem. Int. Ed.* 58 (45) (2019) 16062–16066.
[152] Q.Y. Jia, J.K. Li, K. Caldwell, D.E. Ramaker, J.M. Ziegelbauer, R.S. Kukreja, A. Kongkanand, S. Mukerjee, Circumventing metal dissolution induced degradation of Pt-alloy catalysts in proton exchange membrane fuel cells: Revealing the asymmetric volcano nature of redox catalysis, *ACS Catal.* 6 (2) (2016) 928–938.
[153] P. Strasser, S. Koh, T. Anniyev, J. Greeley, K. More, C.F. Yu, Z.C. Liu, S. Kaya, D. Nordlund, H. Ogasawara, M.F. Toney, A. Nilsson, Lattice-strain control of the activity in dealloyed core-shell fuel cell catalysts, *Nat. Chem.* 2 (6) (2010) 454–460.
[154] H. Nishikawa, H. Yano, J. Inukai, D.A. Tryk, A. Iiyama, H. Uchida, Effects of sulfate on the oxygen reduction reaction activity on stabilized Pt skin/PtCo alloy catalysts from 30 to 80 ℃, *Langmuir* 34 (45) (2018) 13558–13564.
[155] H. Yano, N. Takao, M. Arao, M. Matsumoto, T. Itoh, H. Imai, A. Iiyama, J. Inukai, H. Uchida, Potential cycle-induced change in the crystal structure of a Pt-skin/PtCo alloy nanostructured electrocatalyst for fuel cells, *ACS Appl. Nano Mater.* 2 (12) (2019) 7473–7477.
[156] H. Yano, I. Arima, M. Watanabe, A. Iiyama, H. Uchida, Oxygen reduction activity and durability of ordered and disordered Pt_3Co alloy nanoparticle catalysts at practical temperatures of polymer electrolyte fuel cells, *J. Electrochem. Soc.* 164 (9) (2017) F966–F972.
[157] J. Kim, C.B. Rong, Y. Lee, J.P. Liu, S.H. Sun, From core/shell structured FePt/Fe_3O_4/MgO to ferromagnetic FePt nanoparticles, *Chem. Mater.* 20 (23) (2008) 7242–7245.
[158] Y. Takahashi, T. Kadono, S. Yamamoto, V.R. Singh, V.K. Verma, K. Ishigami, G. Shibata, T. Harano, Y. Takeda, T. Okane, Y. Saitoh, H. Yamagami, M. Takano, A. Fujimori, Orbital magnetic moment and coercivity of SiO_2-coated FePt nanoparticles studied by X-ray magnetic circular dichroism, *Phys. Rev. B* 90 (2) (2014) 024423.
[159] Z.Y. Qi, C.X. Xiao, C. Liu, T.W. Goh, L. Zhou, R. Maligal-Ganesh, Y.C. Pei, X.L. Li, L.A. Curtiss, W.Y. Huang, Sub-4 nm PtZn intermetallic nanoparticles for enhanced mass and specific activities in catalytic electrooxidation reaction, *J. Am. Chem. Soc.* 139 (13) (2017) 4762–4768.
[160] W.S. Jung, B.N. Popov, New method to synthesize highly active and durable chemically ordered fct-PtCo cathode catalyst for PEMFCs, *ACS Appl. Mater. Interfaces* 9 (28) (2017) 23679–23686.
[161] S. Sharma, C. Zeng, A.A. Peterson, Face-centered tetragonal (FCT) Fe and Co alloys of Pt as catalysts for the oxygen reduction reaction (ORR): A DFT study, *J. Chem. Phys.* 150 (4) (2019) 041704.
[162] M.J. Liu, H.L. Xin, Q. Wu, Unusual strain effect of a Pt-based $L1_0$ face-centered tetragonal core in core/shell nanoparticles for the oxygen reduction reaction, *Phys. Chem. Chem. Phys.* 21 (12) (2019) 6477–6484.
[163] M. Watanabe, H. Yano, D.A. Tryk, H. Uchida, Highly durable and active PtCo alloy/graphitized carbon black cathode catalysts by controlled deposition of stabilized Pt skin layers, *J. Electrochem. Soc.* 163 (6) (2016) F455–F463.
[164] Z.X. Wang, X.Z. Yao, Y.Q. Kang, L.Q. Miao, D.S. Xia, L. Gan, Structurally ordered low-Pt intermetallic electrocatalysts toward durably high oxygen reduction reaction activity, *Adv. Funct. Mater.* 29 (35) (2019) 1902987.
[165] R. Wainright, R.P. Ramasamy, Platinum and platinum-cobalt nanowires supported on carbon nanospheres as electrocatalysts for oxygen reduction reaction, *J. Electrochem. Soc.* 163 (6) (2016) F533–F538.
[166] S.M. Alia, S. Pylypenko, K.C. Neyerlin, D.A. Cullen, S.S. Kocha, B.S. Pivovar, Platinum-coated cobalt nanowires as oxygen reduction reaction electrocatalysts, *ACS Catal.* 4 (8) (2014) 2680–2686.
[167] H. Lv, J. Wang, Z. Yan, B. Li, D. Yang, C. Zhang, Carbon-supported Pt-Co nanowires as a novel cathode catalyst for proton exchange membrane fuel cells, *Fuel Cells* 17 (5) (2017) 635–642.
[168] W.P. Xiao, W. Lei, M.X. Gong, H.L. Xin, D.L. Wang, Recent advances of structurally ordered intermetallic nanoparticles for electrocatalysis, *ACS Catal.* 8 (4) (2018) 3237–3256.
[169] H. Yano, M. Kataoka, H. Yamashita, H. Uchida, M. Watanabe, Oxygen reduction activity of carbon-supported Pt-M (M=V, Ni, Cr Co, and Fe) alloys prepared by nanocapsule method, *Langmuir* 23 (11) (2007) 6438–6445.
[170] R.K. Polagani, P.L. Suryawanshi, S.P. Gumfekar, S.H. Sonawane, M. Ashokkumar, Ultrasound-assisted synthesis of Pt–Co/C bimetallic alloys for oxygen reduction in PEM fuel cells, *Sustain. Energy Fuels* 2 (7) (2018) 1491–1499.
[171] M. Chiwata, H. Yano, S. Ogawa, M. Watanabe, A. Iiyama, H. Uchida, Oxygen reduction reaction activity of carbon-supported Pt-Fe, Pt-Co, and Pt-Ni alloys with stabilized Pt-skin layers, *Electrochemistry* 84 (3) (2016) 133–137.
[172] Y.G. Zhao, C. Wang, J.J. Liu, F. Wang, PDA-assisted formation of ordered intermetallic $CoPt_3$ catalysts with enhanced oxygen reduction activity and stability, *Nanoscale* 10 (19) (2018) 9038–9043.
[173] G.-T. Fu, X. Jiang, R. Wu, S.-H. Wei, D.-M. Sun, Y.-W. Tang, T.-H. Lu, Y. Chen, Arginine-assisted synthesis and catalytic properties of single-crystalline palladium tetrapods, *ACS Appl. Mater. Interfaces* 6 (2014) 22790–22795.

[174] J.L. Li, X.N. Fu, Z. Mao, Y.S. Yang, T. Qiu, Q.Z. Wu, Synthesis of PtM (M=Co, Ni)/reduced graphene oxide nanocomposites as electrocatalysts for the oxygen reduction reaction, *Nanoscale Res. Lett.* 11 (1) (2016) 3.
[175] S. Louisia, Y.R.J. Thomas, P. Lecante, M. Heitzmann, M.R. Axet, P.A. Jacques, P. Serp, Alloyed Pt_3M (M = Co, Ni) nanoparticles supported on S- and N-doped carbon nanotubes for the oxygen reduction reaction, *Beilstein J. Nanotechnol.* 10 (2019) 1251–1269.
[176] D. Kaewsai, M. Hunsom, Comparative study of the ORR activity and stability of Pt and PtM (M = Ni, Co, Cr, Pd) supported on polyaniline/carbon nanotubes in a PEM fuel cell, *Nanomaterials (Basel)* 8 (5) (2018) E299.
[177] D. Kaewsai, P. Piumsomboon, K. Pruksathorn, M. Hunsom, Synthesis of polyaniline-wrapped carbon nanotube-supported PtCo catalysts for proton exchange membrane fuel cells: Activity and stability tests, *RSC Adv.* 7 (34) (2017) 20801–20810.
[178] K. Wang, W. Wu, Z.H. Tang, L.G. Li, S.W. Chen, N.M. Bedford, Hierarchically structured $Co(OH)_2$/CoPt/N-CN air cathodes for rechargeable zinc-air batteries, *ACS Appl. Mater. Interfaces* 11 (5) (2019) 4983–4994.
[179] L.N. Chong, J.G. Wen, J. Kubal, F.G. Sen, J.X. Zou, J. Greeley, M. Chan, H. Barkholtz, W.J. Ding, D.J. Liu, Ultralow-loading platinum-cobalt fuel cell catalysts derived from imidazolate frameworks, *Science* 362 (6420) (2018) 1276–1281.
[180] Y.C. Shi, J.J. Feng, X.X. Lin, L. Zhang, J.H. Yuan, Q.L. Zhang, A.J. Wang, One-step hydrothermal synthesis of three-dimensional nitrogen-doped reduced graphene oxide hydrogels anchored PtPd alloyed nanoparticles for ethylene glycol oxidation and hydrogen evolution reactions, *Electrochim. Acta* 293 (2019) 504–513.
[181] K. Huang, P.F. Xu, X. He, R.Y. Wang, Y.G. Wang, H.J. Yang, R. Zhang, M. Lei, H.L. Tang, Annealing-free platinum–cobalt alloy nanoparticles on nitrogen-doped mesoporous carbon with boosted oxygen electroreduction performance, *ChemElectroChem* 7 (15) (2020) 3341–3346.
[182] F.F. Ren, H.W. Wang, C.Y. Zhai, M.S. Zhu, R.R. Yue, Y.K. Du, P. Yang, J.K. Xu, W. S. Lu, Clean method for the synthesis of reduced graphene oxide-supported PtPd alloys with high electrocatalytic activity for ethanol oxidation in alkaline medium, *ACS Appl. Mater. Interfaces* 6 (5) (2014) 3607–3614.
[183] Q. Wang, Y. Tian, G.J. Chen, J.X. Zhao, Theoretical insights into the energetics and electronic properties of MPt_{12} (M = Fe Co, Ni, Cu, and Pd) nanoparticles supported by N-doped defective graphene, *Appl. Surf. Sci.* 397 (2017) 199–205.
[184] V.A. Bogdanovskaya, N.V. Panchenko, M.V. Radina, O.V. Korchagin, V.T. Novikov, Catalysts based on carbon nanotubes modified by N, Pt, or PtCo for oxygen reaction catalysis in nonaqueous electrolyte containing lithium ions, *Mater. Chem. Phys.* 258 (2021) 123856.
[185] A. Zitolo, N. Ranjbar-Sahraie, T. Mineva, J. Li, Q. Jia, S. Stamatin, G.F. Harrington, S.M. Lyth, P. Krtil, S. Mukerjee, E. Fonda, F. Jaouen, Identification of catalytic sites in cobalt-nitrogen-carbon materials for the oxygen reduction reaction, *Nat. Commun.* 8 (1) (2017) 957.
[186] Z.Y. Zhang, Z.P. Li, K.K. Meng, Y. Wu, J.K. Chen, X.G. Xu, Y. Jiang, Perpendicular magnetic anisotropy in $SrTiO_3$/Co/Pt films induced by oxygen diffusion from $CaTiO_3$ spacer layer, *Appl. Phys. Lett.* 116 (23) (2020) 232402.
[187] H.-Y. Chen, H.-J. Niu, Z. Han, J.-J. Feng, H. Huang, A.-J. Wang, Simple fabrication of trimetallic platinum-nickel-cobalt hollow alloyed 3D multipods for highly boosted hydrogen evolution reaction, *J. Colloid Interface Sci.* 570 (2020) 205–211.
[188] Y. Zhuang, J.-P. Chou, P.-Y. Liu, T.-Y. Chen, J.-J. Kai, A. Hu, H.-Y.-T. Chen, Pt_3 clusters-decorated Co@Pd and Ni@Pd model core-shell catalyst design for the oxygen reduction reaction: A DFT study, *J. Mater. Chem. A* 6 (2018) 23326–23335.
[189] C.J. Li, Y. Xu, Y.H. Li, H.R. Xue, Z.Q. Wang, X.N. Li, L. Wang, H.J. Wang, Enhanced dual fuel cell electrocatalysis with trimetallic PtPdCo mesoporous nanoparticles, *Chem. Asian J.* 13 (19) (2018) 2939–2946.
[190] S.R. Zhang, K. An, S.S. Li, Z.Y. Zhang, R.L. Sun, Y. Liu, Bi-active sites of stable and highly dispersed platinum and oxygen vacancy constructed by reducing a loaded perovskite-type oxide for CO oxidation, *Appl. Surf. Sci.* 532 (2020) 147455.
[191] K.A. Kuttiyiel, Y. Choi, K. Sasaki, D. Su, S.M. Hwang, S.D. Yim, T.H. Yang, G.G. Park, R.R. Adzic, Tuning electrocatalytic activity of Pt monolayer shell by bimetallic Ir-M (M=Fe Co, Ni or Cu) cores for the oxygen reduction reaction, *Nano Energy* 29 (2016) 261–267.
[192] Y.J. Sun, B.L. Huang, Y.J. Li, Y. Xing, M.C. Luo, N. Li, Z.H. Xia, Y.N. Qin, D. Su, L. Wang, S.J. Guo, Trifunctional fishbone-like PtCo/Ir enables high-performance zinc–air batteries to drive the water-splitting catalysis, *Chem. Mater.* 31 (19) (2019) 8136–8144.
[193] W.Q. Li, Y.H. Li, H.Q. Fu, G.X. Yang, Q. Zhang, S.Z. Chen, F. Peng, Phosphorus doped Co_9S_8@CS as an excellent air-electrode catalyst for zinc-air batteries, *Chem. Eng. J.* 381 (2020) 122683.
[194] L.M. Rivera Gavidia, G. García, V. Celorrio, M.J. Lázaro, E. Pastor, Methanol tolerant Pt_2CrCo catalysts supported on ordered mesoporous carbon for the cathode of DMFC, *Int. J. Hydrog Energy* 41 (43) (2016) 19645–19655.
[195] S.D. Lankiang, S. Baranton, C. Coutanceau, Electrocatalytic behaviour towards oxygen reduction reaction of carbon-supported $PtxMyAu_z$ (M = Ni, Cu, Co) binary and ternary catalysts, *Electrochim. Acta* 242 (2017) 287–299.
[196] S. Takahashi, N. Todoroki, R. Myochi, T. Nagao, N. Taguchi, T. Ioroi, F.E. Feiten, Y. Wakisaka, K. Asakura, O. Sekizawa, T. Sakata, K. Higashi, T. Uruga, Y. Iwasawa, T. Wadayama, Effective surface termination with Au on PtCo@Pt core-shell nanoparticle: Microstructural investigations and oxygen reduction reaction properties, *J. Electroanal. Chem.* 842 (2019) 1–7.
[197] E. Lohrasbi, M. Javanbakht, S.A. Mozaffari, Effect of atomic composition on the compressive strain and electrocatalytic activity of PtCoFe/sulfonated graphene, *Appl. Surf. Sci.* 407 (2017) 236–245.
[198] H.D. Li, Y. Han, H. Zhao, W.J. Qi, D. Zhang, Y.D. Yu, W.W. Cai, S.X. Li, J.P. Lai, B.L. Huang, L. Wang, Fast site-to-site electron transfer of high-entropy alloy nanocatalyst driving redox electrocatalysis, *Nat. Commun.* 11 (1) (2020) 5437.
[199] L.T. Song, J.Q. Chang, Y.H. Ma, X.H. Tan, Y.Q. Xu, L.M. Guo, Z.X. Chen, T.Q. Zhao, Y.Q. Li, Y.L. Liu, Y. Zhang, W.G. Chu, Cobalt/nitrogen codoped carbon nanosheets derived from catkins as a high performance non-noble metal electrocatalyst for oxygen reduction reaction and hydrogen evolution reaction, *RSC Adv.* 10 (71) (2020) 43248–43255.
[200] Y. Zheng, S. Chen, H.Y. Lu, C. Zhang, T.X. Liu, 3D honeycombed cobalt, nitrogen co-doped carbon nanosheets *via* hypersaline-protected pyrolysis towards efficient oxygen reduction, *Nanotechnology* 31 (36) (2020) 364003.
[201] P. Zhu, J.X. Gao, S. Liu, Facile *in situ* coupling CoFe/Co nanoparticles and N-doped carbon nanotubes/graphitic nanosheets as bifunctional oxygen electrocatalysts for rechargeable Zn-air batteries, *J. Power Sources* 449 (2020) 227512.
[202] M.C. Qian, X.Y. Cheng, T.T. Sun, J.N. Tian, T.T. Isimjan, Z.F. Shi, X.L. Yang, Synergistic catalytic effect of N-doped carbon embedded with CoFe-rich $CoFe_2O_4$ clusters as highly efficient catalyst towards oxygen reduction, *J. Alloys Compd.* 819 (2020) 153015.
[203] F.J. Li, Y. Yin, C. Zhang, W.J. Li, K. Maliutina, Q.L. Zhang, Q.X. Wu, C.X. He, Y. Zhang, M. Yang, L.D. Fan, Enhancing oxygen reduction performance of oxide-CNT through *in situ* generated nanoalloy bridging, *Appl. Catal. B Environ.* 263 (2020) 118297.
[204] J.B. Tan, T. Thomas, J.X. Liu, L. Yang, L.H. Pan, R. Cao, H.J. Shen, J.C. Wang, J. Liu, M.H. Yang, Rapid microwave-assisted preparation of high-performance bifunctional Ni_3Fe/Co-N-C for rechargeable Zn-air battery, *Chem. Eng. J.* 395 (2020) 125151.
[205] L.G. Feng, R.F. Ding, Y.W. Chen, J.W. Wang, L. Xu, Zeolitic imidazolate framework-67 derived ultra-small CoP particles incorporated into N-doped carbon nanofiber as efficient bifunctional catalysts for oxygen reaction, *J. Power Sources* 452 (2020) 227837.
[206] B.Y. Song, S. Yao, Optimization of sulfurization process of cobalt sulfide and nitrogen doped carbon material for boosting the oxygen reduction reaction catalytic activity in alkaline medium, *Front. Chem.* 8 (2020) 314.